Fracture of skin-stiffener intersections in composite wind turbine blade structures
by Darrin John Haugen

A thesis submitted in partial fulfillment of the requirements for the degree of Master of Science . in Mechanical Engineering
Montana State University

Abstract:
Most wind turbine blades have a stiffening spar running the length of the blade to add rigidity to the airfoil skins. This spar is usually an I-beam or C-channel. The interface between the spar flange and skin surface is often the site of fracture and delamination growth in composite wind turbine blades. Fracture initiates here due to high out-of-plane stresses and stress concentration areas, combined with the low transverse and out-of-plane strength of composite materials. Areas such as the stiffener flange tip may develop stress singularities due to the geometric mismatch between the flange and skin that cannot be analyzed with standard strength-based criteria. These factors make skin-stiffener detail regions a critical design component in wind turbine blade structures.

The goals for this study were to combine experimental testing with finite element analysis (FEA) to establish design guidelines and develop an accurate FEA method for predicting skin-stiffener fracture loads and locations.

Experimental fracture toughness tests showed that delamination growth resistance was higher for cracks propagating at a (+45/-45) degree ply interface than for cracks between two (0) degree plies. Increasing the skin bending stiffness and matrix material toughness produced large increases in pull-off loads. Increasing the flange thickness and the adhesive bond-line thickness caused the damage location to change from the web/flange bend region to the flange tip. This was due to the increasing geometric discontinuity at the flange tip, which created high interlaminar stresses.

A strength-based failure prediction with FEA results was adequate to predict damage onset in the stiffener specimens in regions without high stress gradients. However, a fracture mechanics approach was necessary to analyze the flange tip region. Good agreement with experimental damage onset loads was obtained by using the one-step virtual crack closure technique (VCCT-1) to calculate strain energy release rate values, which were used with the linear interaction criterion for crack growth to predict propagation loads. An initial crack length of less than 0.2 mm and a crack length to crack extension ratio (a/da) of greater than 20 provided good results for the modeling of damage onset at the flange tip.

FRACTURE OF SKIN-STIFFENER INTERSECTIONS IN COMPOSITE WIND TURBINE BLADE STRUCTURES

by

Darrin John Haugen

A thesis submitted in partial fulfillment
of the requirements for the degree

of

Master of Science

in

Mechanical Engineering

MONTANA STATE UNIVERSITY-BOZEMAN
Bozeman, Montana

August 1998

APPROVAL

of a thesis submitted by

Darrin John Haugen

This thesis has been read by each member of the thesis committee and has been found to be satisfactory regarding content, English usage, format, citations, bibliographic style, and consistency, and is ready for submission to the College of Graduate Studies.

Dr. Douglas Cairns Douglas A. Cairns 7/7/98
Chairperson, Graduate Committee Date

Approved for the Department of Mechanical Engineering

Dr. Vic Cundy Vic A. Cundy 7/7/98
Department Head Date

Approved for the College of Graduate Studies

Dr. Joseph Fedock Joseph J. Fedock 7/10/98
Graduate Dean Date

STATEMENT OF PERMISSION TO USE

In presenting this thesis in partial fulfillment of the requirements for a master's degree at Montana State University-Bozeman, I agree that the Library shall make it available to borrowers under rules of the Library.

If I have indicated my intention to copyright this thesis by including a copyright notice page, copying is allowable only for scholarly purposes, consistent with "fair use" as prescribed in the U.S. Copyright Law. Requests for permission for extended quotation from or reproduction of this thesis in whole or in parts may be granted only by the copyright holder.

Signature Dan Hemp

Date 7/7/98

ACKNOWLEDGMENTS

I gratefully acknowledge the guidance of Dr. Douglas Cairns and Dr. John Mandell in this research effort. Their support throughout my graduate career has made this project possible. Thanks are directed to Dr. Jay Conant for serving as a graduate committee member. Daniel Samborsky deserves special recognition for all of the assistance with experimental testing, manufacturing, data analysis, and preparing figures and photographs for this report. Thanks to the other graduate students in the composite materials group for your smiles and friendships over the past few years. Finally, thanks to my family, and most of all, Melissa, my wife. Your never ending support and love have helped me to attain my goals and strive to always do my best.

This work was supported by the U.S. Department of Energy and the State of Montana through the Montana DOE EPSCoR Program (Contract # DEFC02-91ER75681) and Sandia National Laboratories (Subcontract ANO412).

TABLE OF CONTENTS

LIST OF TABLES

LIST OF FIGURES

ABSTRACT

Most wind turbine blades have a stiffening spar running the length of the blade to add rigidity to the airfoil skins. This spar is usually an I-beam or C-channel. The interface between the spar flange and skin surface is often the site of fracture and delamination growth in composite wind turbine blades. Fracture initiates here due to high out-of-plane stresses and stress concentration areas, combined with the low transverse and out-of-plane strength of composite materials. Areas such as the stiffener flange tip may develop stress singularities due to the geometric mismatch between the flange and skin that cannot be analyzed with standard strength-based criteria. These factors make skin-stiffener detail regions a critical design component in wind turbine blade structures.

The goals for this study were to combine experimental testing with finite element analysis (FEA) to establish design guidelines and develop an accurate FEA method for predicting skin-stiffener fracture loads and locations.

Experimental fracture toughness tests showed that delamination growth resistance was higher for cracks propagating at a (+45/-45) degree ply interface than for cracks between two (0) degree plies. Increasing the skin bending stiffness and matrix material toughness produced large increases in pull-off loads. Increasing the flange thickness and the adhesive bond-line thickness caused the damage location to change from the web/flange bend region to the flange tip. This was due to the increasing geometric discontinuity at the flange tip, which created high interlaminar stresses.

A strength-based failure prediction with FEA results was adequate to predict damage onset in the stiffener specimens in regions without high stress gradients. However, a fracture mechanics approach was necessary to analyze the flange tip region. Good agreement with experimental damage onset loads was obtained by using the one-step virtual crack closure technique (VCCT-1) to calculate strain energy release rate values, which were used with the linear interaction criterion for crack growth to predict propagation loads. An initial crack length of less than 0.2 mm and a crack length to crack extension ratio (a/da) of greater than 20 provided good results for the modeling of damage onset at the flange tip.

CHAPTER 1

INTRODUCTION

Improvements in wind turbine blade structures and design methods are essential for continued advancement in the utilization of wind power as a viable energy resource. Blades must sustain complicated fatigue loading, extreme event static loading, and be damage tolerant to meet their projected lifetime goals. In addition, there is a trade off among increasing blade strength and lifetime, while decreasing blade efficiency due to added weight.

To meet these performance requirements, most wind turbine blades now use composite materials. Composite materials consist of a reinforcing phase, such as glass or carbon fibers, and a binder phase, usually a thermoset or thermoplastic polymer. Composites are the preferred material due to their combination of high in-plane strength in the fiber direction, good fatigue resistance, and high stiffness to weight ratio. However, they are quite weak in the transverse and out-of-plane (through-thickness) directions. Longitudinal and transverse properties for a unidirectional E-glass fabric/polyester composite are listed in Table 1. Note the much lower values for strengths and moduli in the transverse (UTS_T, E_T) and through thickness (UTS_Z, E_Z) directions compared to the longitudinal fiber direction (UTS_L, E_L). As a result, transverse

Table 1. Longitudinal and transverse properties for unidirectional polyester/E-glass composite (D155 fabric at a V_F of 36%) [1].

Property	Test Values	Average	Std. Dev.
E_L (GPa)	28.1, 27.0, 29.8	28.3	1.4
E_T (GPa)	8.00, 7.31, 7.93	7.75	0.38
E_Z (GPa)	7.10, 7.65, 7.38	7.38	0.28
UTS_L (MPa)	891, 814, 883, 838	856.0	37.0
UTS_T (MPa)	26.6, 36.0, 30.4, 32.9, 29.0	31.0	3.6
UTS_Z (MPa)	21.7, 18.7, 20.4, 18.1	19.7	1.6

cracking and peeling apart of the ply layers are common failure modes.

Most wind turbine blades use a span-wise stiffening spar (Fig. 1) that is bonded to the inner skin surfaces to stiffen the blade, prevent skin bucking, resist transverse shear loading, and provide the proper natural frequency of vibration for the blade. It has been observed that failure is often the result of skin-stiffener separation in composite skin-stiffened structures [2, 3]. The geometric changes in these areas lead to high stress gradients, complex stress variations, and significant interlaminar stresses, which cause delamination failure.

Kedward et al. [4] reported that many composite structure failures have been the result of "detail design oversights", especially at curved regions, and that designers have

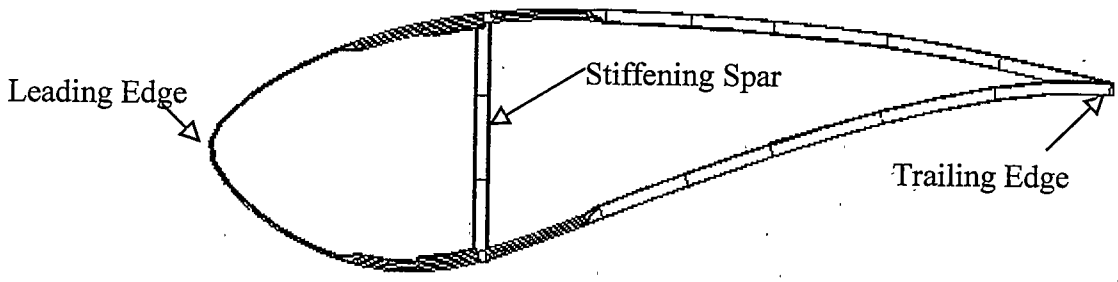

Figure 1. Wind turbine blade cross section.

a "general lack of appreciation" for the low through-thickness strengths of composites. According to Martin [3], global analysis approaches "fail to identify those areas, such as structural or material discontinuities, where failure will initiate from interlaminar stresses." In addition, design details are subject to processing variability and are difficult to inspect once inserted in a blade. Consequently, these detail regions have limited the performance and lifetimes of blades.

In order to investigate the mechanisms of fracture in these detail regions, an approach combining experimental testing of blade detail regions with finite element analysis (FEA) was used. The goals were to establish design guidelines for composite skin-stiffener detail regions and to formulate an accurate predictive capability and design methodology with FEA, especially at geometric discontinuities such as the flange tip. Once better predictive ability is established it should reduce the dependence on expensive structural testing [3], helping the design engineer to optimize detail region performance.

CHAPTER 2

BACKGROUND

Problems with Stiffener Detail Regions

Stiffened composite skins are a widely used engineering structure. Besides the current application in wind turbine blades, skin-stiffener structures are utilized in nearly all aircraft fuselage designs. A primary failure mode for these detail regions is delamination. This is due to a number of factors relating to material properties, design methodology, and load transfer paths.

Skin-stiffener intersections are inherently difficult to design due to the combination of multiple loading conditions and stress concentration areas. Some of these stress concentration areas, such as the flange tip, produce interlaminar stresses that act in the weakest plane of the composite material. It has been found that a stress singularity can exist at the flange terminus [5, 6, 7] implying that a stress component grows unbounded in this region. Analysis of these stress zone singularities can be difficult, requiring techniques that are not common practice for most designers. However, they are not impractical and have been implemented in the study of composite structures [3, 7-13] by previous investigators. A standard design method is to use a strength-based approach for calculating initial damage in areas where no stress singularity is present. This is

followed by a fracture mechanics analysis to predict delamination growth. If a singular stress field is present special design approaches are required from the outset. These techniques are discussed in detail in Chapter 4.

Stiffener Design Considerations

Some of the major problems and design concerns relating to composite stiffener designs have been addressed in the literature and are summarized in the remainder of this section. The topics of interest are as follows: flange tip taper angle, skin/flange bending stiffness and bending stiffness ratio, delamination interface ply orientations and bonding, matrix material selection, through-thickness reinforcements, manufacturing issues, and bend radii in curved composite parts.

Flange Taper Angle

Many composite structures contain geometric discontinuities that produce through-thickness (peeling) stresses even when the loading is entirely in-plane. Some common features that display this behavior are shown in Figure 2. In stiffener detail regions, this singular stress zone occurs at the flange tip (Fig. 3) and has been noted by Hyer and Cohen [5, 6, 7] and Kassapoglou [11]. Tapering the flange tip (Fig. 3) has been shown to dramatically increase the pull-off strength of composite stiffeners. This happens because the interlaminar peel and shear stresses and stress gradients are reduced at the flange tip area by minimizing the geometric and stiffness discontinuity,

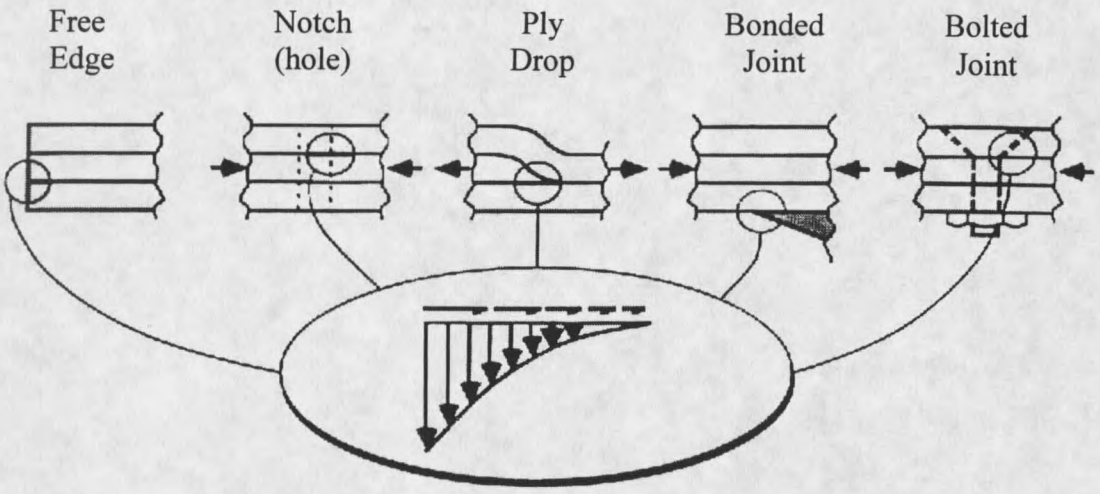

Figure 2. Structural discontinuities producing high stress gradients [14].

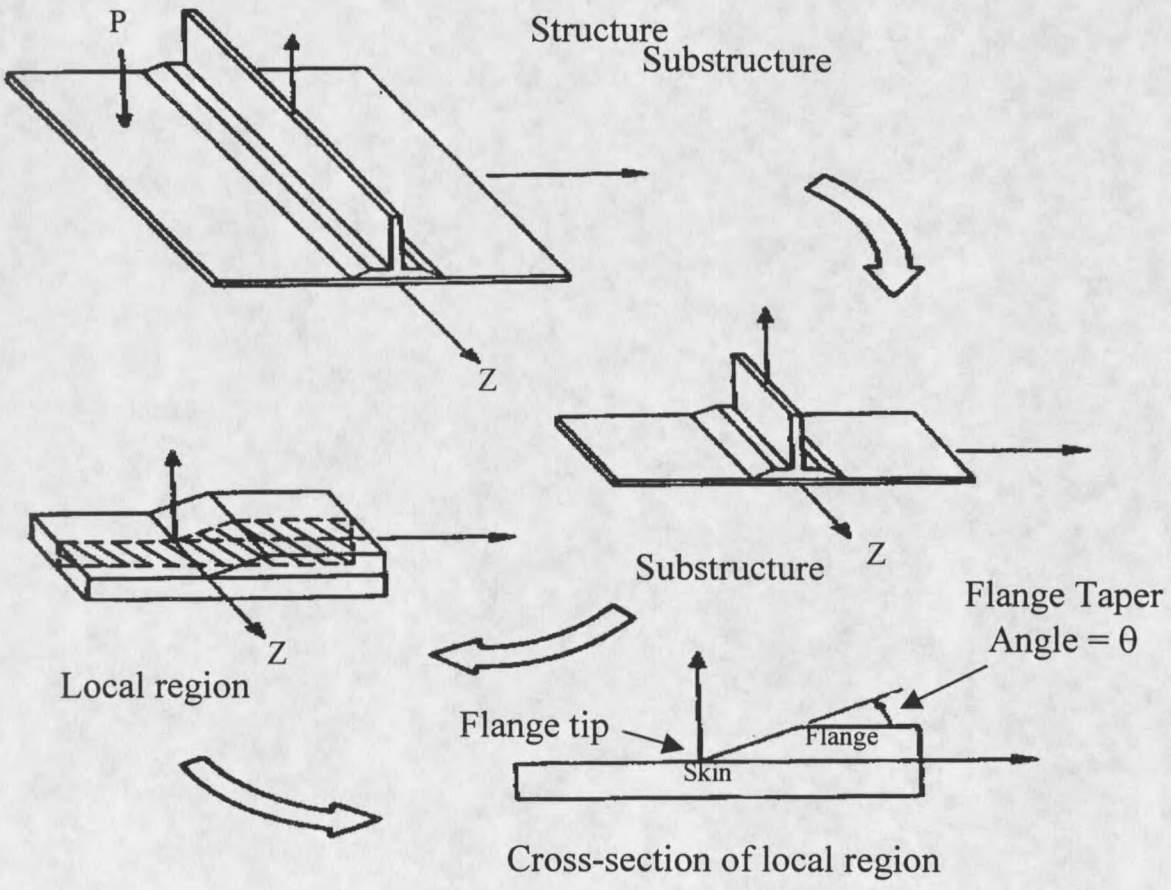

Figure 3. Skin-stiffener global-local structures and flange tip region [7].

effectively reducing the stresses [5, 6]. Minguet et al. [15] noted this increased performance of samples with tapered flange tips in stiffener pull-off tests. A 32% higher initial damage onset load for a 20^0 taper, coMPared with a 45^0 taper was observed. Minguet and O'Brien [9] noted a 35% increase in damage initiation load for samples with a 20^0 taper angle versus a 90^0 flange tip in 3-point bending tests. Furthermore, a detailed finite element solution at the flange tip confirmed that the tapered configuration reduced the peel stress by 76%, thus explaining the load increase at fracture onset. Tapering the flange tip clearly mitigates one of the main causes of delamination onset in composite stiffeners.

Skin and Flange Bending Stiffness

Another design aspect that has received attention is the bending stiffness in the skin and flange and the relative stiffness ratio between these components. Much of this work has been in response to the "pressure pillowing" effect seen in aircraft fuselage structures. Pressure pillowing occurs in fuselage structure during the cabin pressurization procedure when the internal cabin pressure makes the skin bulge outward in between the rows of stiffeners attached to the skin. This condition leads to bending in the skin transverse to the stiffener longitudinal axis. As a result, peeling and transverse shear stresses develop at the interface between the skin and stiffener. This same loading may be encountered in wind turbine blades if there is localized skin buckling producing chord-wise bending near the stiffener. Minguet et al. [15] reported a significant increase in strength with an increase in skin flexural stiffness in skin/stringer pull-off tests. Their data showed a 95% increase in maximum load with a 30% increase in skin thickness and

initial damage moment values increased approximately 66% with the 30% increase in skin thickness. Kassapoglou [11] utilized elasticity solutions to evaluate the parameter of flange to skin bending stiffness (thickness) ratio with all 0^0 unidirectional material in both the skin and flange. For the case of in-plane skin tensile stress applied perpendicular to the stiffener longitudinal axis, thin flanges performed better. As flange/skin thickness ratio (t_f/t_s) increased the damage onset load went through a minimum, and then began to increase (Fig. 4). According to this data, t_f/t_s ratios of 0.5 to 1.5 should be avoided since they had the lowest predicted failure onset loads for flange tip failure. For skin in-plane

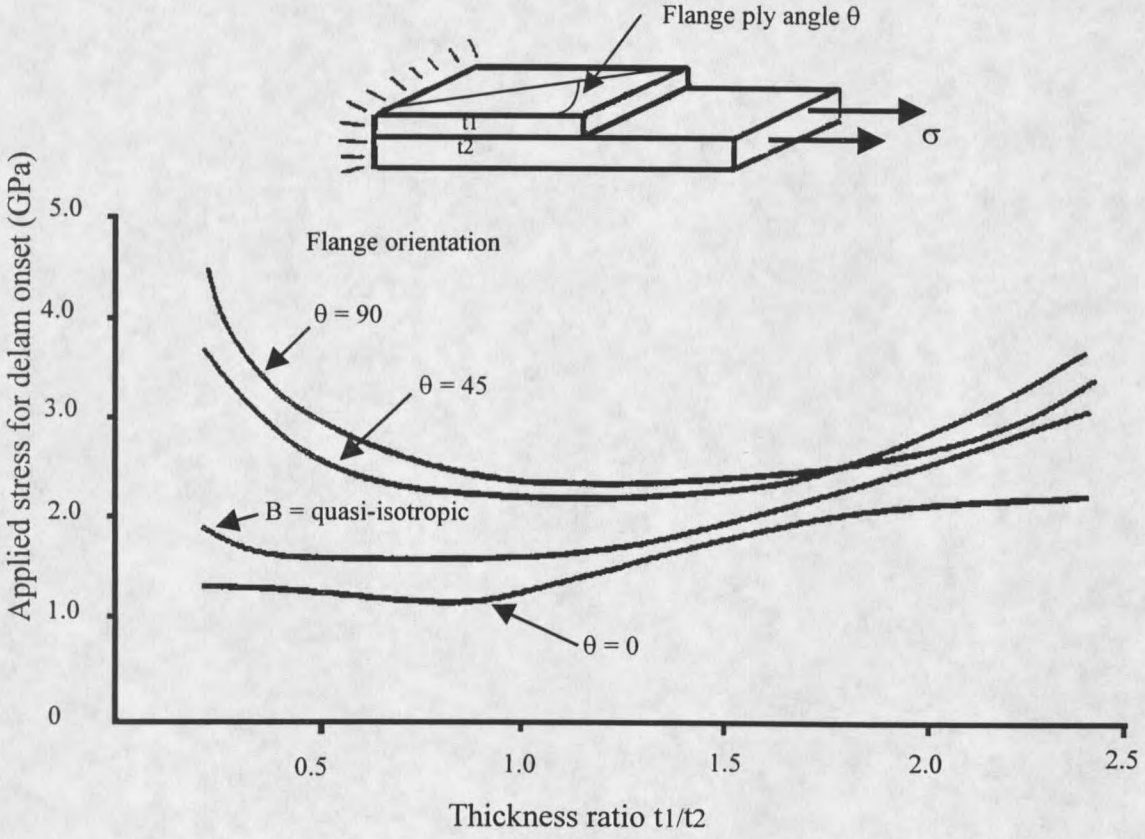

Figure 4. Delamination onset stress vs. flange lay-up and flange/skin thickness ratio [11].

shear loading the highest delamination onset loads occurred below a ratio of 0.5, with lower ratios performing better (Fig. 5).

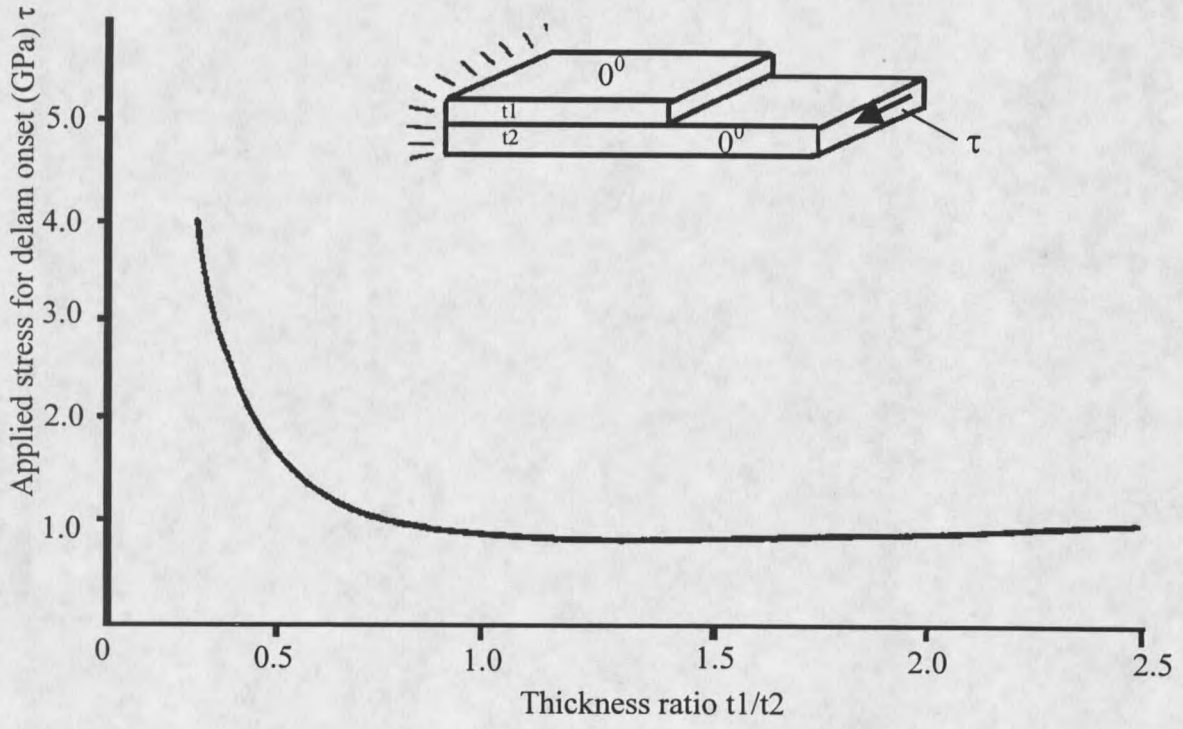

Figure 5. Onset of delamination for skin and flange under shear [11].

Delamination Interface Ply Angles

The relative angle of the composite plies at the delamination interface has also received some attention. Minguet and O'Brien investigated failure onset for the case of skin bending simulating pressure pillowing effects [8]. Results indicate that 90^0 plies at the bondline are the worst case, due to the propensity to form transverse cracks that initiate delaminations. Kassapoglou [11] used elasticity solutions to predict behavior of a flange/skin strip (Fig. 4) loaded with a tensile stress in the skin applied perpendicular to

the stiffener longitudinal axis. For the case of a unidirectional skin aligned with the tension loading and $t_f/t_s < 1.0$, higher in-plane flange stiffness (in the load direction) produced lower delamination onset loads (Fig. 4). Kassapoglou explained this behavior by noting that increasing the flange stiffness (or thickness) increased the load carried by the flange. This creates moments between the skin and flange that must be balanced by a moment at the flange tip. That moment is generated by development of high interlaminar stresses in that area.

Variations in delamination resistance with varying ply angle and fabric architecture have also been noted for stitched and woven fabrics typical of those used by the wind turbine industry. Scott [16] found that in double cantilever beam (DCB) tests for a polyester/E-glass fabric system, G_{Ic} increased from 490 J/m^2 for a $[(0)]_{10}$ sample to 780 J/m^2 for a crack at a (0/+45) interface. He also found increases in G_{IIc} with ply interface lay-up. For five-harness satin orthogonal woven carbon/epoxy DCB samples with 12K tow bundles, Alif et al. [17] found that G_{Ic} increased when coMPared with a unidirectional sample. This was attributed to the crack path following the weave topology since no fiber bridging was observed in the woven fabric samples. As a result, this woven architecture requires more energy input to grow a crack than for self-similar planar crack growth observed at unidirectional interfaces. Based upon the previous references, it appears that designers can build delamination resistance into stiffener intersections through proper lay-up selection for a particular loading case.

Matrix Material

It is widely known that delamination is highly dependent on matrix material

properties [18, 19]. When composite plies are peeled apart, the behavior is influenced by the fracture toughness of the matrix. Bradley [19] reported that composite G_{Ic} was actually greater than neat resin G_{Ic} for resin toughness values below 500 J/m^2. As resin toughness was increased, composite toughness increased. However, once resin toughness was at or above 2000 J/m^2 he found very little increase in overall composite toughness. This was attributed to the resin fracture process zone size being constrained by the adjoining fiber layers, with the zone size being on the order of the inter-ply spacing. Minguet et al. [15] observed that delaminations in bonded skin-stiffener pull-off tests never propagated within the adhesive layer itself, but grew within the top-most skin ply. In this case, the adhesive was tougher than the base resin system and therefore, had a higher resistance to crack growth. The delamination preferentially found the easiest path for advancement. If the resin formulation were toughened, this weak link could be reduced or eliminated from stiffener designs.

Through-thickness Reinforcement

Another method used in composite manufacturing to prevent delamination growth is through-thickness reinforcements. These are usually in the form of stitching or 3-D fiber weaves. This is done to strengthen the composite laminate in its out-of-plane direction, which can have a strength value of as little as 3% of its in-plane tensile strength [4]. Stitching and riveting have proven effective at improving delamination resistance, but when used at greater areal percentages, reduce in-plane tensile strength due to net-section loss [20, 21]. Mignery et al. [21] studied stitching as a means to deal with free edge delamination problems in tensile coupons. They discovered that one row of

stitching at each free edge had mixed effects on in-plane tensile strength, but effectively arrested delamination growth as the crack approached the stitch line. In addition, they performed FEA to investigate the strain energy release rate (SERR) and interlaminar normal stress distribution. The interlaminar normal stress was relatively unchanged by adding stitching, however, as the crack approached the stitch line, the SERR decreased, explaining the delamination arrest. This is due to the stitching restraining through-thickness displacement at the crack tip, which is referred to as fiber bridging.

A commercially available through-thickness reinforcement called Z-fiber™ has shown promise at increasing fracture toughness in composites. Z-fiber™ consists of short sections of either carbon fiber or 0.5 mm diameter titanium pins contained in a foam sheet in a "bed of nails" configuration. The foam is crushed on top of a fabric preform, pushing the pins into the fabric through the thickness. Typical reinforcing percentages are from 1 to 5% by area. Freitas and Fusco [20] report that Mode I fracture toughness for composites may increase by up to 50 times when coMPared with an unreinforced sample. Small decreases in ultimate in-plane tensile strain values were observed for AS4/3501-6 woven carbon fabric samples. When 5% areal density 0.5 mm titanium Z-fiber™ was used to reinforce skin-stringer pull-off sample, maximum pull-off loads were 2.5 times higher than the co-cured baseline sample. Improvements to Mode II shear delamination resistance are still under investigation. The main drawback to this technology appears to be cost. It is marketed toward the aerospace industry, and may not be feasible for low-cost wind turbine applications, or other large structures.

Design for Manufacturing

In order to meet the low-cost manufacturing goals for wind turbine blades, a number of manufacturing methods have been investigated. A primary method under consideration at MSU-Bozeman is resin transfer molding (RTM). In RTM resin is pumped through a closed mold cavity filled with dry fabric preform and allowed to cure.

A common design issue with RTM'd stiffeners has been web/flange transition fillet radius [4, 22]. Holmberg and Berglund found that the inner radius of RTM U-beams (C-channels) was an area of high fiber volume, reduced local permeability during resin flow, increased voids, and highly variable strength [22]. This was due to the fabric pulling tight around the fillet radius in the mold cavity. They also reported that literature values for recommended radii were between 3-12 mm for the RTM process. From U-beam strength testing they observed better performance for larger fillet radius beams. Beams with a 5.0 mm radius displayed average initial fracture loads (per unit width) in the bend region of 13.1 N/mm and 20.3 N/mm for vacuum bag and press forming methods, respectively. Beams with a 0.8 mm radius had an average initial damage load of approximately 10.3 N/mm for both manufacturing methods. The strength differences were due to a higher radial tensile stress in the bend of the 0.8 mm radius beams coMPared with the 5.0 mm radius beams at equal loading. Based upon these results, it appears that increasing the web fillet radius lowers the stress concentration in this area. This should increase the damage onset load at this detail region for stiffener geometries that are prone to delamination in the web-flange fillet radius area. However, there is a trade-off between lower stress concentrations through a larger fillet radius and added

material and weight in this region.

Fracture Mechanics

The field of fracture mechanics was developed to deal with the issues that are specific to materials containing cracks. Once a crack has formed in a material, standard stress-based analysis can no longer be accurately used to predict material yielding and crack advancement. Linear elastic fracture mechanics predicts that the elastic stress field perpendicular to the crack plane becomes unbounded at the crack front [23]. This is due to the existence of a $1/\sqrt{r}$ stress singularity at the crack tip [23], where r is the radial distance from of the crack tip.

Cracks may be loaded in the three distinct modes shown in Figure 6.

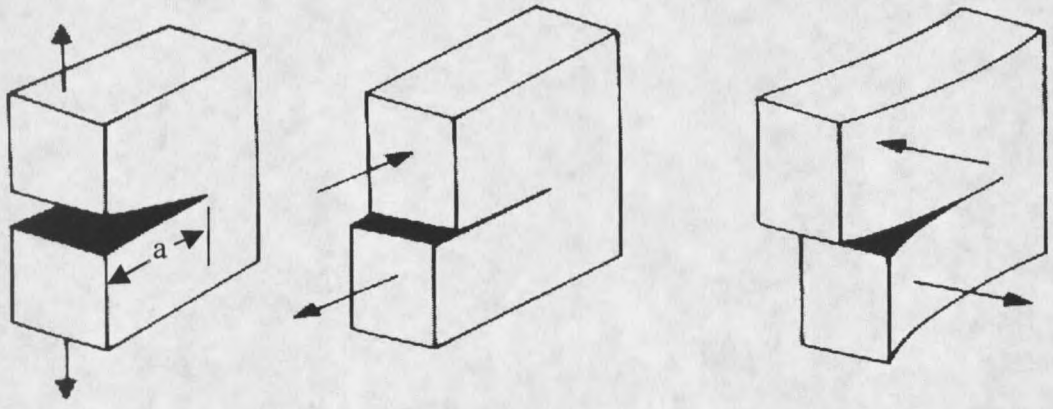

Figure 6. The three modes of crack loading [23].

Mode I is a pure opening mode, caused by stresses acting normal to the crack plane. Mode II is an in-plane shear mode, and Mode III is an out-of-plane shearing mode.

Strain Energy Release Rate

One of the most common methods of analyzing and predicting crack behavior is the concept of strain energy release rate (SERR or G). The basis for the SERR lies in the Griffith criterion, which states, "crack propagation will occur if the energy released upon crack growth is sufficient to provide all the energy that is required for crack growth" [23]. The condition for crack growth is as follows:

$$dU/da = dW/da \qquad (1)$$

where U = elastic strain energy

W = energy required for crack growth

a = crack length

G is also called the crack driving force and equals dU/da. The crack growth resistance is referred to as R and equals dW/da, which is the energy consumed in crack propagation per unit area of crack extension. The condition for growth in Equation (1) can also be read as G = R at crack extension. At or above some critical value of G, the crack will propagate. This critical value must be experimentally determined for different material systems for each of the three crack extension modes. The critical value usually differs for each mode and is denoted with subscripts as G_{Ic}, G_{IIc}, G_{IIIc}, respectively. In practical terms, materials that are "tougher" have a higher value of G_c, requiring more energy to grow a crack in that material. A detailed discussion of fracture mechanics principles is

presented by Broek in Reference [23].

Experimental Determination of Strain Energy Release Rate

To obtain critical values for G in static loading conditions, a variety of tests are used for the various modes of crack extension. For Mode I fracture, the standard test specimen is the double cantilever beam (DCB) as described in ASTM standard D 5528 [24] and shown in Figure 7. A composite DCB sample is made by placing a thin film

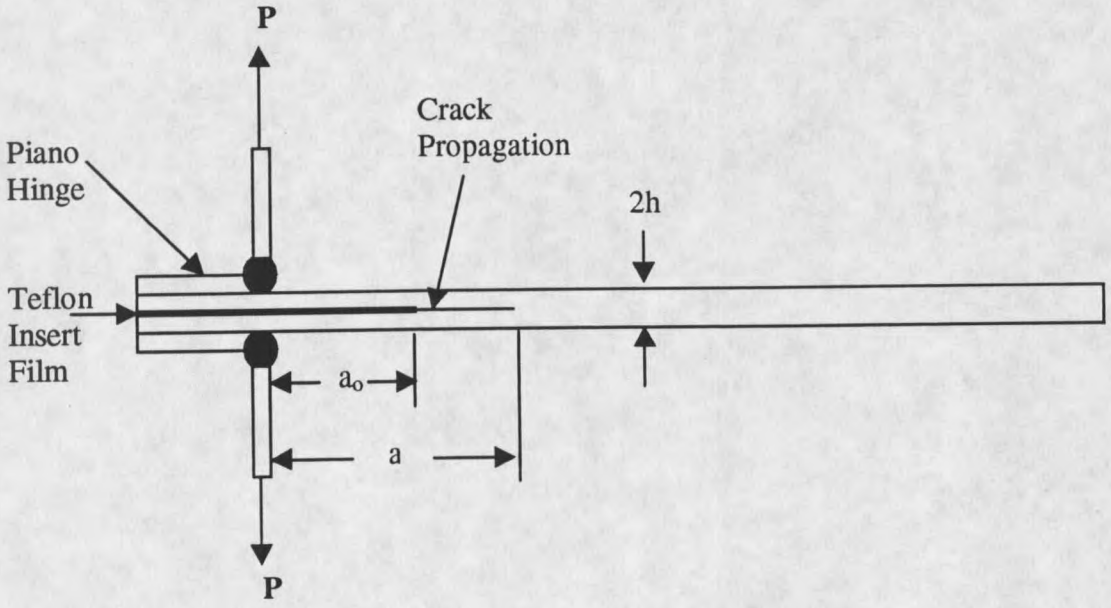

Figure 7. DCB geometry and loading.

of "release paper", usually Teflon film, at the mid-plane of a laminate. This insert film serves as a delamination initiation site for the crack. The critical strain energy release rate to grow a crack in the material can be obtained by the use of the output load vs. displacement curve (Fig. 8) and the modified beam theory (MBT) method (Eq. 2).

$$G_{Ic} = 3P\delta / 2ba \qquad (2)$$

Where: P = critical load at crack propagation

δ = displacement between DCB cantilever arms at critical load

b = sample width

a = crack length

Another method, called the area method [18], needs a loading-unloading path plot (Fig. 8) for each G_{Ic} calculation. By calculating the area enclosed by the curve (strain energy released during the test) and dividing by the crack extension area, G_{Ic} may be calculated. This is shown as Equation (3). A drawback with the area method is that it

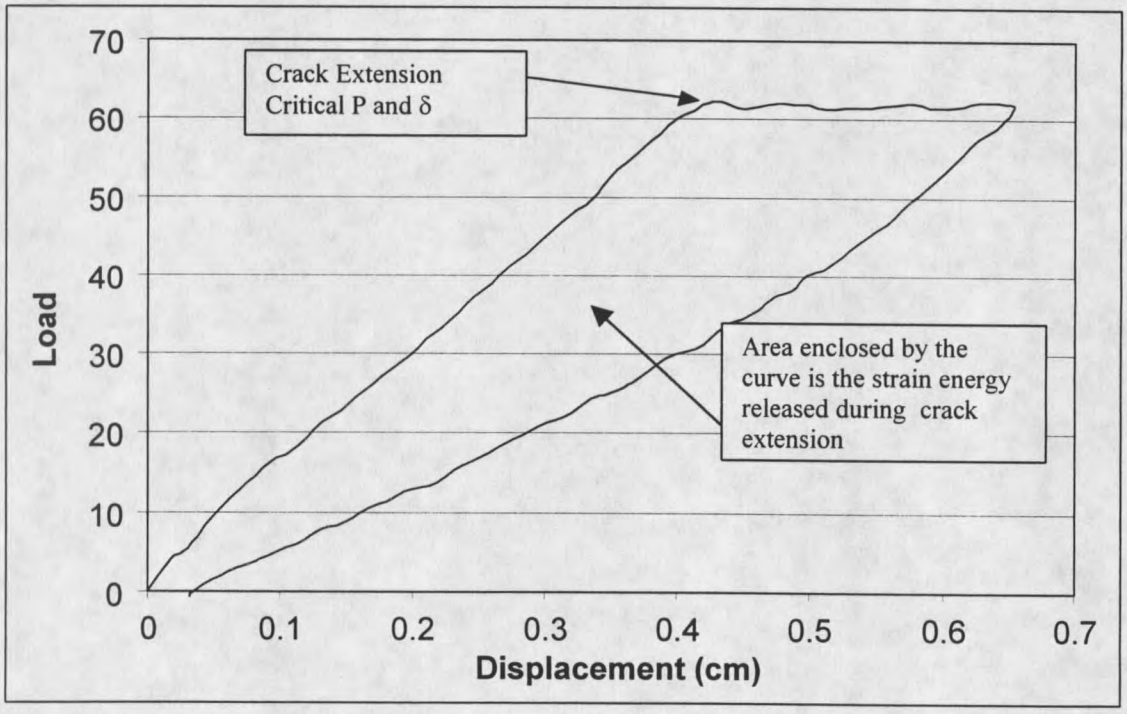

Figure 8. Typical loading-unloading curve for DCB test.

$$G_{Ic} = \text{Area} / b(a_2 - a_1) \qquad (3)$$

Where: Area = area enclosed by loading/unloading curve

b = sample width

a_1 = initial crack length

a_2 = final crack length

will not give an initiation value for G_{Ic} from the Teflon insert film as recommended by ASTM D 5528.

The end-notched flexure (ENF) test has emerged as the standard test method for calculating critical SERR in Mode II type crack growth. Typical specimen geometry and loading for an ENF sample is shown in Figure 9. This sample produces shear at the

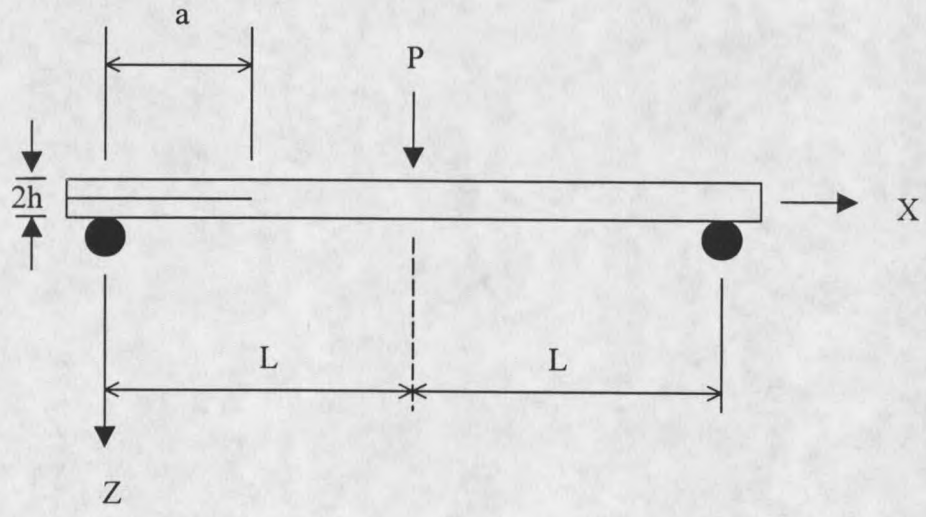

Figure 9. ENF geometry and loading.

mid-plane of a composite specimen loaded in three-point bending. When a critical load is reached, the crack advances, usually in an unstable manner [16]. A formula used to

calculate G_{IIc} based on beam theory [25, 26] is presented as Equation 4.

$$G_{IIc} = 9P^2 a^2 C / 2b(2L^3 + 3a^3) \quad (4)$$

Where: P = critical load at propagation

a = initial crack length

C = specimen compliance

b = sample width

L = one-half support spacing distance

Analytical Prediction of Strain Energy Release Rate

Many analytical methods have been developed for use with finite element analysis (FEA) to predict strain energy release rates in each mode of crack extension. Two popular ways to calculate G are by (1) calculating the change in strain energy in an FEA model with an associated crack extension (virtual crack extension – VCE) [25], and (2) calculating the energy required to close a crack front by a small increment (virtual crack closure technique – VCCT) [8, 10, 12, 13, 21, 28-30]. Both methods have gained acceptance, but the virtual crack closure technique has emerged as the preferred method. It has the benefit of allowing separate G calculations for each mode of crack extension.

The VCCT is based upon Irwin's hypothesis that the energy absorbed during crack extension (da) is equal to the work done to close that crack by the same incremental amount. This is the concept of the crack closure integral [23, 28]. Rybicki and Kanninen [28] applied this concept to the calculation of strain energy release rates with the finite element model. It has subsequently been expanded for use with most common element

types in FEA [29, 30].

The VCCT can be applied by two different methods. The one-step VCCT (VCCT-1) only requires one finite element run to calculate the SERR. This has obvious benefits in saving computing time for detailed analyses with long solution times. In this method, the forces at the crack tip are multiplied by the displacements behind the crack tip. Different formulas have been derived for the various finite elements [30]. A schematic of VCCT-1 for a 2-dimensional 8-node quadrilateral element formulation is presented in Figure 10. The formulas for G_I and G_{II} from reference [30] are presented as Equations (5) and (6) where u and v are the nodal displacements in the x and y directions.

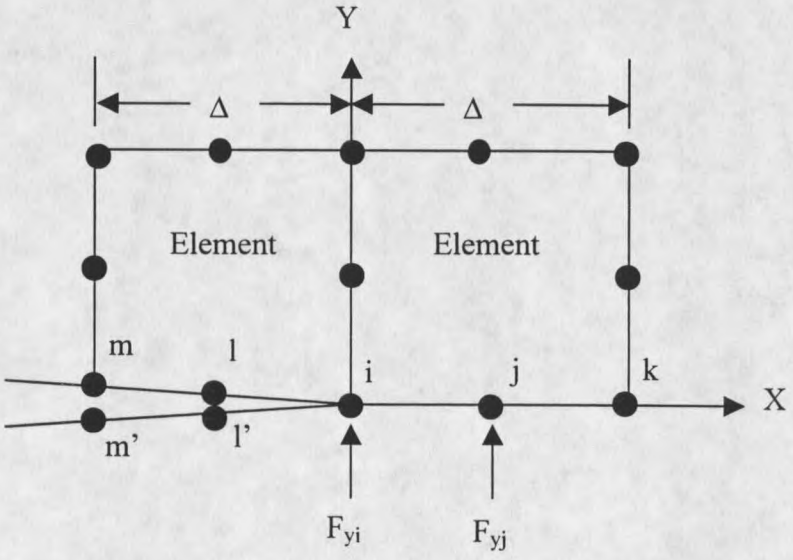

Figure 10. VCCT-1 schematic with 8-node quadrilateral elements.

$$G_I = -1/(2\Delta)[F_{yi}(v_m - v_{m'}) + F_{yj}(v_l - v_{l'})] \quad (5)$$

$$G_{II} = -1/(2\Delta)[F_{xi}(u_m - u_{m'}) + F_{xj}(u_l - u_{l'})] \quad (6)$$

This technique may be used with a variety of element types and does not require the use of a quarter point nodal placement element with a stress singularity at the crack tip. No stresses are used in the calculation and it may be utilized with a relatively coarse mesh. Rybicki and Kanninen [28] found good results for the calculation of stress intensity factors with the VCCT-1 method and constant-strain elements at ratios of crack length to crack extension (a/da) as low as five (5). Martin [3] has reported that when using the VCCT-1 technique, there was no mesh size dependency if the crack was grown within the same material type, but found that if the crack grew at a bimaterial interface, the calculations were mesh size dependent. However, he gave no recommendations for acceptable (a/da) ratios. Values for (a/da) ratios from 50 to 200 have been recommended for general fracture mechanics analysis with FEA [27].

The two step VCCT (VCCT-2) uses two successive FEA runs (Fig. 11) to

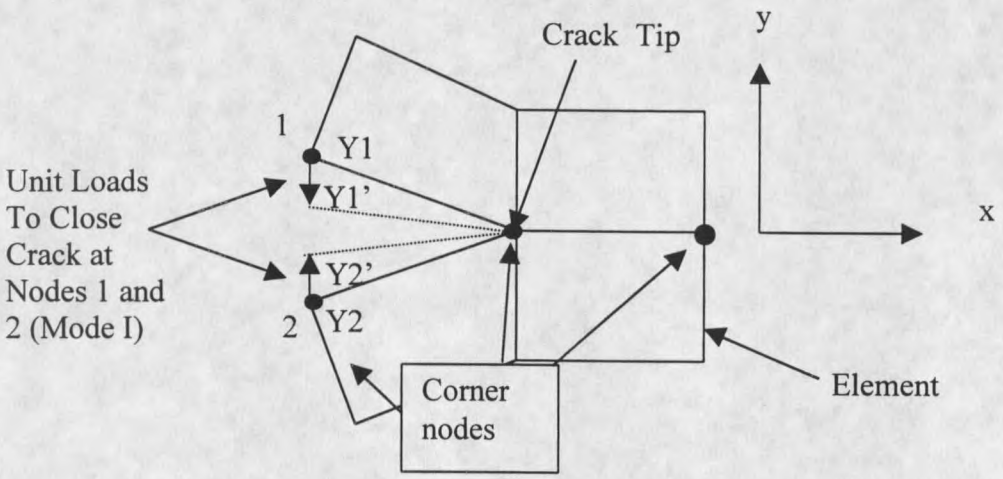

Figure 11. VCCT-2 schematic for Mode I closure.

calculate G values. The first analysis is performed with the specified loading on the structure, while the second analysis uses unit loads at the nodes immediately behind the crack front to close the crack by some amount. The elements at the crack tip are shown in detail in Figure 11. The corresponding formulas to calculate G in Mode I and Mode II are given as Equations (7) and (8), where Y' and X' denote the displacements after the unit loads are applied to close the crack.

$$G_I = \frac{\frac{(Y_1 - Y_2)^2}{(Y_1 - Y_2) - (Y'_1 - Y'_2)}}{2(Element\ width)} \qquad (7)$$

$$G_{II} = \frac{\frac{(X_1 - X_2)^2}{(X_1 - X_2) - (X'_1 - X'_2)}}{2(Element\ width)} \qquad (8)$$

By examining the displacements with the unit loads, one can calculate the force required to completely close the crack by some length (da). In Figure 11, the loads are placed at the corner nodes for an element type without mid-side nodes. The unit loads may be placed at the mid-side nodes if a higher order element is used. This would reduce the length of the crack extension by one half for a given element size and the element width term in the denominator of Equations (7) and (8) would be replaced by one half the element width. This term should more appropriately be labeled the crack closure length (da), depending on the element type used.

Jerram [31] first reported utilizing this technique with constant strain elements. Hellen and Blackburn [32] had errors of up to 20% in predictions for G when using this

technique with higher order elements. This method will be investigated further in Chapter 6, which deals with FEA results from this study.

Mode Interaction and Failure Criteria

The previous developments for experimental and analytical methods can be combined to perform predictive work with fracture mechanics in composite structures. To do so, designers must understand how crack growth interaction occurs when more than one mode of crack extension is present. In the following development, Mode III is not included because it was not observed in the experimental substructure tests.

Many investigators have recently addressed mixed-mode delamination in composite structures. The development of the mixed-mode bending test (MMB) to calculate G values with mixed-mode loading has facilitated this research [17, 26, 33, 34]. The MMB test allows for any mixed percentage of Mode I and/or Mode II growth to be achieved simultaneously, and for the critical G value in each mode at propagation to be calculated. Mixed-mode interaction criteria for predictive work with FEA can then be developed.

As mentioned previously, a crack will advance when G equals G_c in a particular mode. When a mode mix is present, the following general form of interaction has been proposed [26] for combined Mode I and II growth (Eq. 5). The key to the implementation

$$(G_I/G_{Ic})^{m/2} + (G_{II}/G_{IIc})^{n/2} = 1 \qquad (5)$$

of Equation (5) has been finding the best exponents m and n to match the experimental behavior for particular material systems. According to Reeder [35], a value of two is

most often used in the literature for both m and n. This makes the overall exponent for each term one, and gives the common and easily implemented "linear interaction criterion". A linear interaction is pleasing from a theoretical point of view since strain energy release rate is a scalar quantity. A graphical representation of the linear interaction criterion is shown in Figure 12. Russell and Street [26] found good agreement

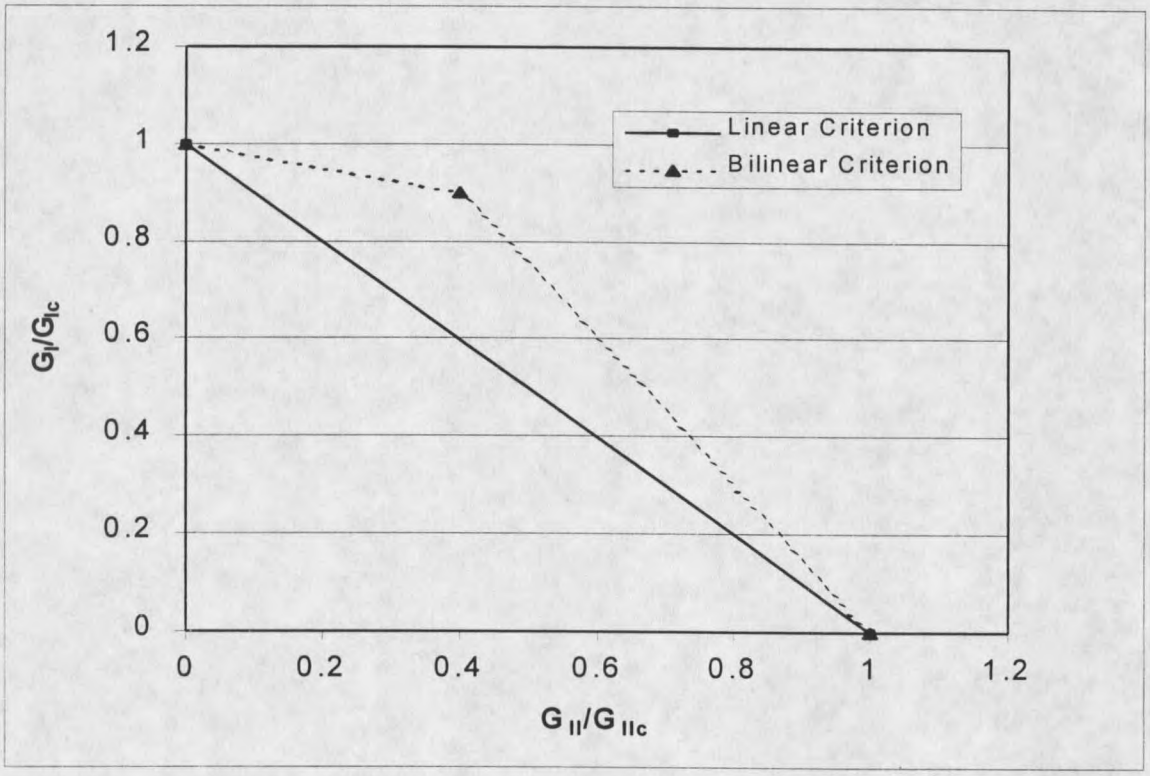

Figure 12. Generalized graphical representation of the linear and bilinear failure criteria.

between predictions and test results for unidirectional graphite/epoxy prepreg samples using the linear interaction criterion. In addition, Alif et al. [17] observed mixed mode behavior in a woven fabric carbon/epoxy laminate that followed a linear relation between G_{Ic} and G_{IIc}. However, Reeder [35] and Konig et al. [33] have found that a bilinear

failure criteria works better for some material systems due to the observed increase in G_{Ic} at certain intermediate mode ratios in the vicinity of $G_I/G_{II} = 1$ [35]. This is shown graphically in Figure 12. In particular, Reeder found the bilinear criterion gave better predictions for carbon/epoxy systems. He also found that systems with tougher thermoplastic matrices followed the linear criterion better and recommended testing of MMB samples to see which criteria a particular material will follow.

The implementation of these developments into predictive work with FEA is fairly straightforward [3]. The first step is the establishment of an accurate material toughness database for the material under consideration. Next, an FEA model of the problem is produced and a technique such as the VCCT-1 method is used to calculate the strain energy release rates at that particular load. Once the G values are found, a suitable interaction criterion may be used to predict delamination growth. The actual load to propagate a delamination may then be calculated from the interaction criterion and the fact that the SERR values increase with the square of the applied load in FEA calculations. Thus, load may be scaled appropriately so that the interaction criterion for crack growth is satisfied. This overall global-local design process with FEA is presented as a flowchart in Figure 13. The procedure for using fracture mechanics to predict delamination propagation loads is presented in more detail for designers and analysts in Appendix A.

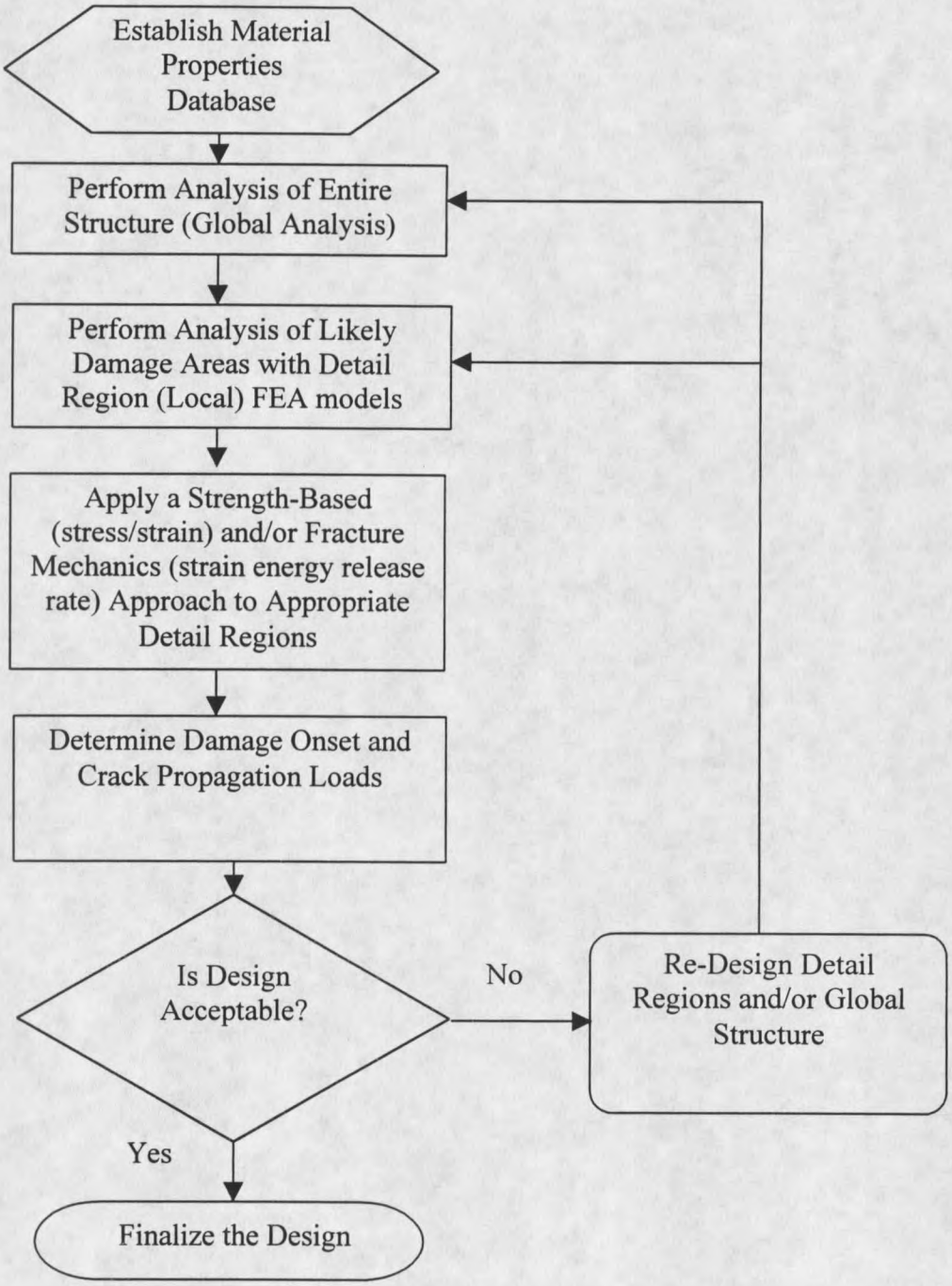

Figure 13. Design flowchart for global-local analysis with FEA.

CHAPTER 3

EXPERIMENTAL METHODS

Materials and Manufacturing

There were two main categories of specimens investigated in this study. The first group was comprised of DCB and ENF specimens as described in Chapter 2. These specimens were used to collect basic delamination data for various fabrics and interface lay-up configurations. The second group consisted of specimens that represented blade substructures in the skin-stiffener detail regions. These specimens were tested using different loading conditions, manufacturing methods, resin materials, geometries, and fabric lay-ups.

All specimens tested were manufactured at MSU-Bozeman using Resin Transfer Molding (RTM). In RTM, dry fabric preform is placed in a mold cavity, and catalyzed resin is then pumped through the cavity space. Once the mold has completely filled, the process stops, and the resin is allowed to cure. The cured composite is removed from the mold cavity after 24 hours, and post-cured at 60^0 C for two hours to ensure full cross-linking of the thermoset polymer matrix.

A Polyester/E-glass system was used for most of the specimens tested in this investigation. This material system is representative of the low-cost materials used by the wind turbine industry. CoRezyn unsaturated orthophthalic polyester (63-AX-051), made

by Interplastic Corporation, with 2% MEKP (by volume) added as a catalyst, was the primary resin used in this study. In addition, a few specimens were made with polyester/PET (PET P460-06) from Alpha Owens-Corning (AOC), and polyurethane (Polytek Poly 15-D65) matrices for comparative purposes. The reinforcing E-glass fabric was an Owens-Corning (Knytex) stitched D155 fabric for the 0^0 layers in all specimens. The weft unidirectional D155 has an areal weight of 526 g/m^2. The (+45/-45) fabric used was the stitched DB120; also from Owens-Corning, with an areal weight of 407 g/m^2.

DCB and ENF Specimens

The DCB and ENF specimens were manufactured as flat plates with a Fluoro-Peel Teflon release film at the mid-plane to serve as the crack initiation film. Three lay-ups were tested. They were $[(0)]_{10}$ at 36 % fiber volume percentage (V_f), $[(0)_2/(45/-45)/(45/-45)/(0)_2]$ at 34 % V_f, and $[(45/-45)]_{10}$ at 26 % V_f. Both specimen types were cut from flat plates with a diamond blade saw to a standard specimen size of 2.54 cm in width, by 17.8 cm in length.

The DCB specimens had 2.54 cm wide stock piano hinges bonded to both faces with Hysol EA 9302.2NA adhesive for the load application points (Fig.7). Specimen and hinge bonding surfaces were sanded with 240 grit sand-paper and wiped clean before adhesive application. In order to get an initiation value for G_{Ic} right from the starter film tip as recommended by ASTM D 5528 [24] the specimens were not pre-cracked. Tests were performed by loading and unloading the specimens so that both the MBT and the Area Method test results could be calculated for each test as outlined in Chapter 2. Crack growth was measured at the end of each test by using a marker dye to penetrate the crack,

clearly showing the crack tip. The crack length was then measured from the load application points and recorded. The crack growth front was generally uniform across the specimen width. In this way, the final crack length for the area method and the initial crack length for the following test were determined. Tests were performed at different crack lengths for each specimen which enabled investigation of R-Curve behavior for Mode I crack growth.

The critical load and displacement for use in the equations in Chapter 2 were determined by the sudden change in slope or the onset of non-linearity in the load-displacement curves (Fig.8) to ensure conservative values for G_{Ic}. These points were selected from the load-displacement curves and entered into the equations as the critical load and displacement values for the MBT method. The area enclosed by the curve was determined by choosing nine key data point sets from the curve and calculating the area with a simple computer program. To validate this calculation, some curves were scanned into a photo-analyzing program at high resolution to calculate the pixels enclosed in the graph. The enclosed area was determined and the two methods were found to agree within 5 percent.

The critical load for the ENF specimens was taken as the onset of non-linearity in the load-displacement curve. In the ENF test, the load increased until a slight non-linearity occurred followed by a large unstable crack advancement (Fig.14). Because of this, only one value of G_{IIc} was obtained for each ENF specimen, and no R-Curve behavior could be investigated.

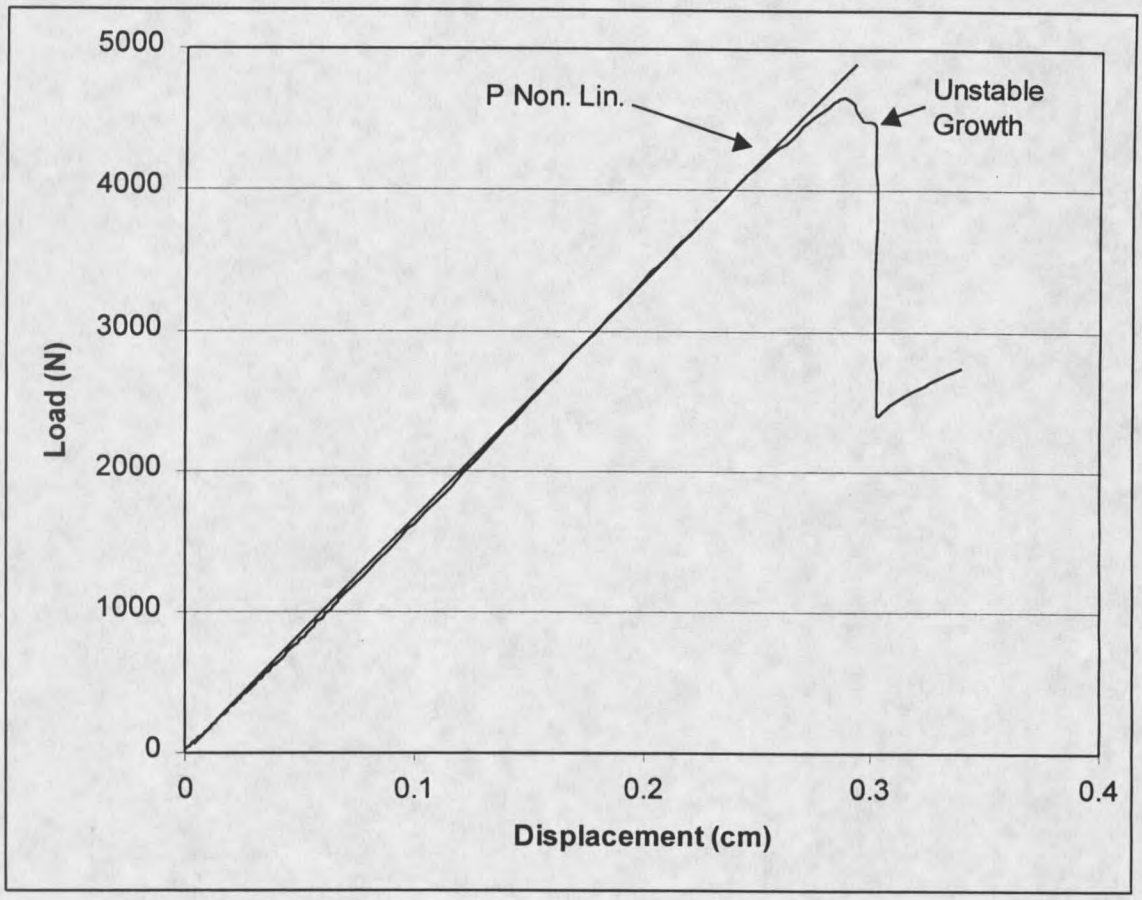

Figure 14. Typical load-displacement curve for ENF test.

Substructure Testing

A variety of tests were performed to investigate the mechanisms and modes of fracture for skin-stiffener intersection detail regions. The test specimens varied in stiffener geometry, materials, delamination interface lay-up, skin and flange stiffness, manufacturing method, and loading cases. A list of the lay-up schedule used for the skin and flange for each specimen type is presented in Table 2. A summary of the test matrix and a description of the various specimen types are presented in Table 3. These tests also provided data for substructure modeling validation with the ANSYS finite element code.

Table 2. Ply orientations and laminate identification codes for substructure tests.

Laminate Configuration*	**ID Code**
Thin-flanged Specimens	
$[+45/-45/0_2/+45/-45]_2$	S1 (skin)
$[+45/-45/0_2/+45/-45]$	F1 (flange)
Thick-flanged Specimens	
$[+45/-45/0_2/+45/-45]$	S2 (skin)
$[90/0/+45/-45]_s$	S3 (skin)
$[(+45/-45/0_2/+45/-45/0_2/+45/-45)_s/+45/-45/0_2/+45/-45]$	F2 (flange)
$[(90/0_2/+45/-45/0_2/+45/-45)_s/+45/-45/0_2/+45/-45]$	F3 (flange)
$[+45/-45/0_2/+45/-45]_s$	Web (used in all specimens)

*Thick-flanged lay-ups include $[+45/-45/0_2/+45/-45]$, which is half of the web lay-up continued onto the top of the flange cap section.

Two different T-mold configurations were used to produce the skin-stiffener specimens. The geometry and loading for the first batch of specimens, referred to as the "thin-flanged" specimens, is shown in Figure 15. The diagram for the "thick-flanged" specimens is displayed in Figure 16. The different designs were utilized to investigate specimens displaying different failure modes. The thin-flanged specimens were expected to display initial damage at the web-flange fillet region, followed by delamination toward the flange tip. In contrast, the thick-flanged specimens were anticipated to fail at the flange tip area, with a delamination then progressing toward the web centerline. The ability to predict this different failure behavior for different geometries could then be established with the FEA models.

The thin-flanged stiffeners were manufactured two ways. They were either co-cured in the mold with the skin, or secondarily bonded to the skin with an adhesive. The secondary bonded type was molded with a layer of release film at the skin and stiffener

Table 3. T specimen substructure test matrix.

Geometry From Table 2		Manufacturing					
Flange	**Skin**	**Bonding**	**Matrix Material**	**Delamination Interface Lay-up**	**Loading**	**# Specimens**	**Motivation**
Thin-flanged Stiffeners							
F1	S1	Co-cured	Polyester	(+45/-45)	Tension	11	Baseline pull-off specimens, investigate damage initiation and growth
F1	S1	Co-cured	Polyester	(+45/-45)	Compression	3	Investigate compressive behavior and damage location
F1	S1	Secondary Bonded (0.15 mm bond) (Hysol Epoxy)	Polyester	(+45/-45)	Tension	12	Investigate performance changes with secondary bonding of skin to stiffener
F1	S1	Variable Bond Thickness (Hysol Epoxy)	Polyester	(+45/-45)	Tension	11	Investigate performance changes with variable bond-line thickness
F1	S1	Secondary bonded (Plexus Methacrylate)	Polyester	(+45/-45)	Tension	6	Investigate bonding of commonly used commercial adhesive
F1	S1	Co-cured	Polyester/PET	(+45/-45)	Tension	4	Investigate delamination resistance of different matrix materials
F1	S1	Co-cured	Polyurethane	(+45/-45)	Tension	3	
Thick-flanged Stiffeners							
F2	S2	Co-cured	Polyester	(+45/-45)	Tension	6	Investigate specimens exhibiting flange tip failures, vary the skin stiffness and interface lay-up
F3	S3	Co-cured	Polyester	(0/0)	Tension	3	

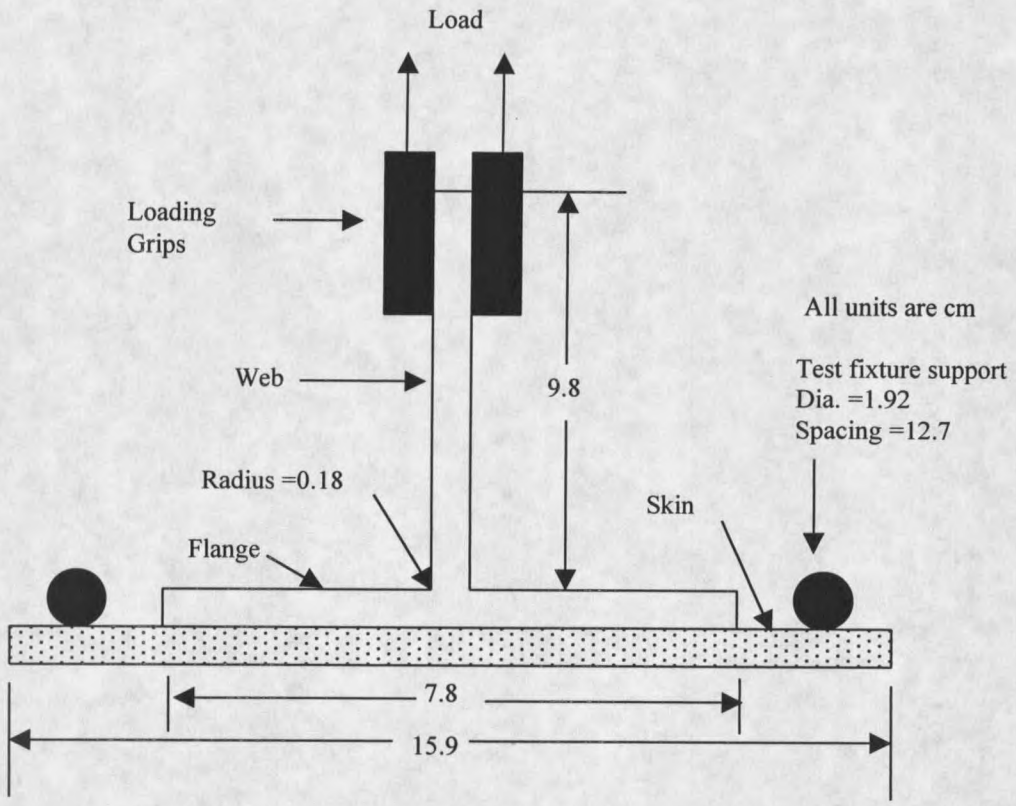

Figure 15. Geometry and loading for thin-flanged stiffener tests.

intersection. The flange and skin cured in the same mold, but did not bond together due to this film layer. To investigate bonding issues, two different adhesives were compared, and the bond-line thickness was varied considerably. The adhesives used were the Hysol EA 9309.2NA and ITW Plexus methacrylate (A0425).

Three different resin systems were compared for relative delamination resistance in static pull-off tests. The resins used were CoRezyn polyester, the polyester/PET blend from Alpha Owens-Corning, and the polyurethane made by Polytek. These resins were expected to have vastly different toughness values allowing investigation of performance changes with different matrix formulations.

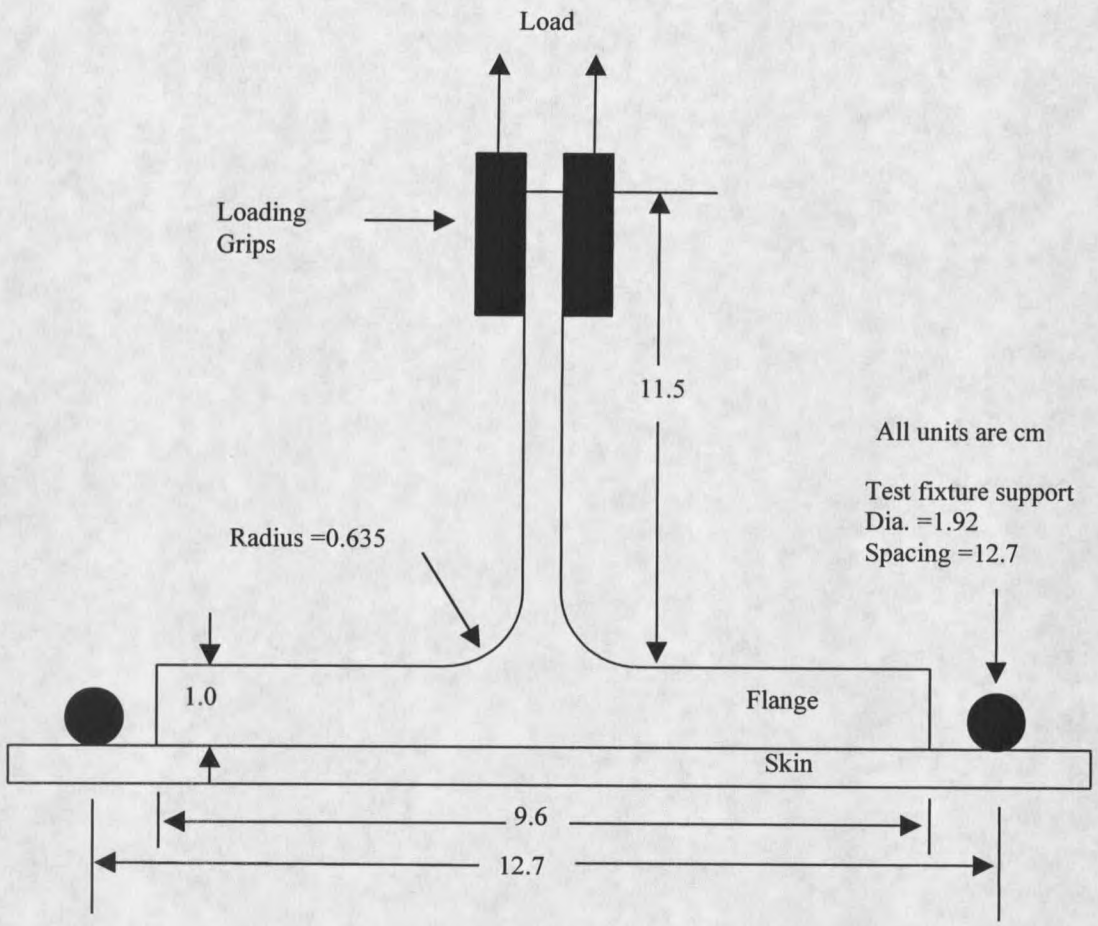

Figure 16. Geometry and loading for thick-flanged stiffener tests.

Flange and skin ply lay-ups were varied to track influences of bending stiffness and delamination interface lay-up on stiffener performance for the thick-flanged specimens. In addition, by varying the interface plies, FEA predictions could be validated more thoroughly, since toughness has been observed to change with delamination ply interface orientation [16].

Two different load cases were applied to the stiffener specimens. They were static tensile pull-off loading, and static compressive loading. These tests were

performed on the simply supported testing apparatus shown in Figure 17. The load was applied to the specimen by gripping the upper 2.5 cm of the web in the hydraulic grips

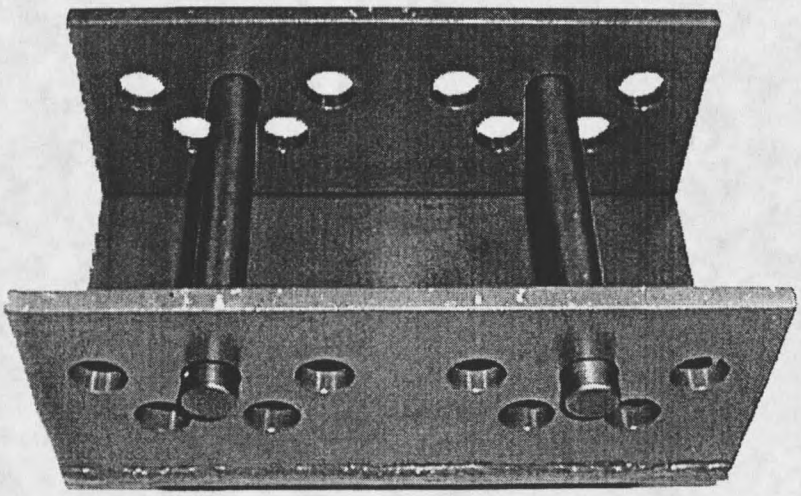

Figure 17. Simply supported test fixture for tensile and compressive stiffener tests.

and reacting the load with the bars in the test fixture (Fig. 17). Support spacing was 12.7 cm for all stiffener tests.

The static pull-off tests were performed in displacement control mode on an Instron 8562 servo-electric testing machine. Data was collected and graphed for load vs. actuator displacement (Fig. 18). In addition, initial fracture load, maximum load, and maximum displacement were manually recorded to verify each plot used in subsequent analysis and to compare specimen performance. Initial damage onset was taken as the point where either the load-displacement curve became non-linear, or the load suddenly dropped by more than 2.6 N/cm. This correlated well with audible and visual damage onset values.

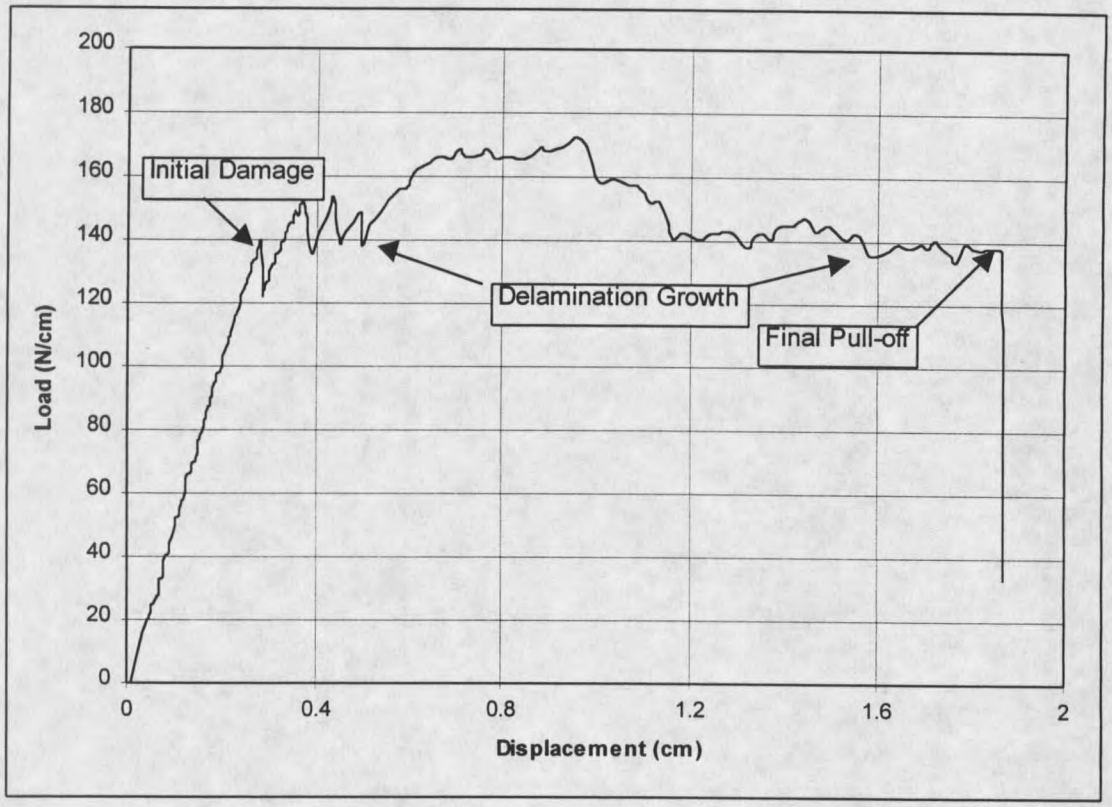

Figure 18. Typical load-displacement curve for thin-flanged stiffener pull-off test.

The static compressive tests were performed in the same testing apparatus, except that the specimen was placed on top of the support bars in the fixture and pushed downward. Initial damage loads, maximum loads, and maximum displacements were recorded from visual and audible observations to compare with the output load-displacement graphs. The onset of non-linearity in the load-displacement curve (Fig. 19) was interpreted as the initial damage load.

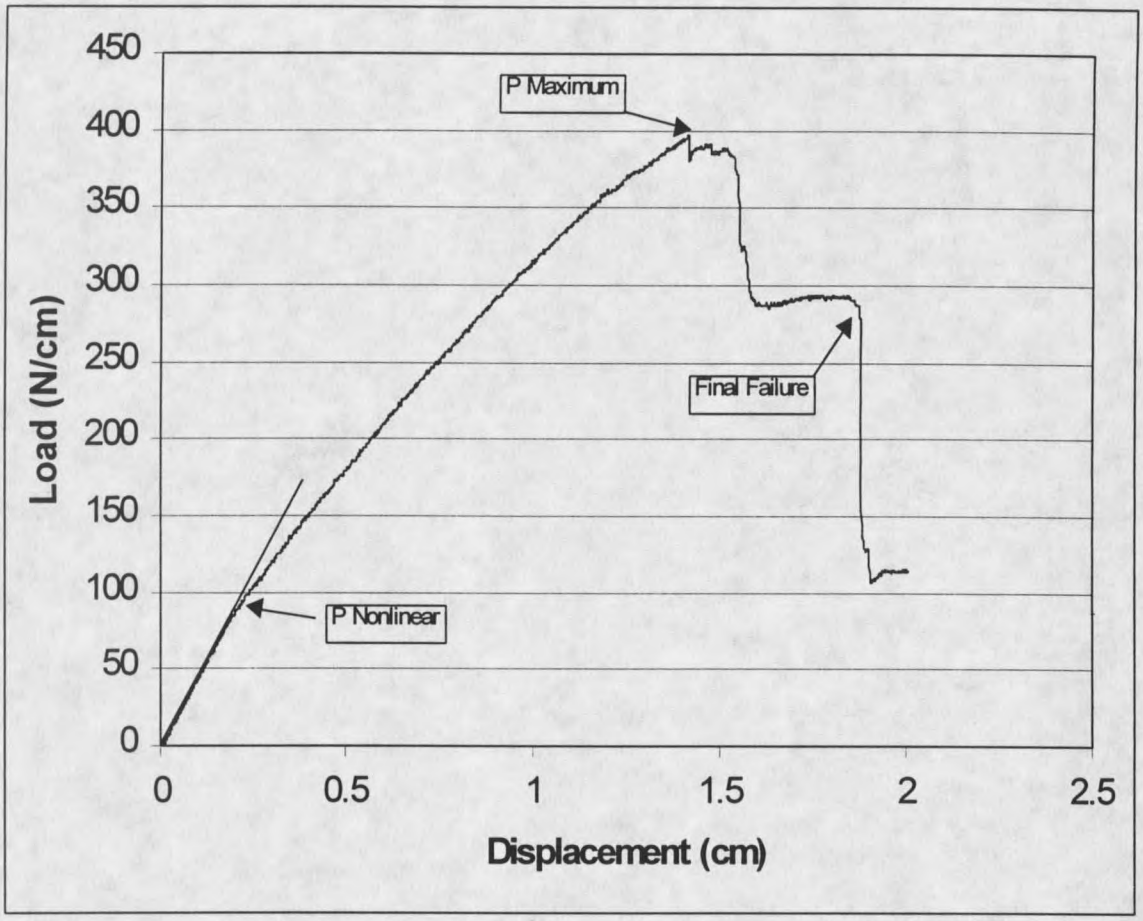

Figure 19. Typical load-displacement curve for compressive thin-flanged stiffener test.

CHAPTER 4

NUMERICAL METHODS

Finite element analysis (FEA) has been established as an indispensable tool for research and design work in the various fields of engineering. It allows structural designers to investigate the effects of parameters such as geometry, material, and loading on design performance. When performed correctly, FEA may drastically reduce the dependence on expensive substructure and full scale experimental testing during the design development process [3].

However, FEA is not a substitute for a thorough understanding of the underlying engineering principles, such as material behavior, failure theories, or fracture mechanics. These principles must be properly applied, and the FEA input and output properly interpreted, to give accurate and meaningful results. In fact, it is commonplace for the first handful of analyses for a design to be incorrect until refinements are made in such areas as mesh sizing, boundary conditions, loading, and inclusion of nonlinear effects. In addition, reliance on FEA results should only come as a result of experience gained by validation with experimental testing. Once benchmark studies have been performed, confidence in the analysis procedures is attained. In this way, FEA reduces the reliance on experimental testing over the long term.

The overall approach of this research follows an experimental/numerical validation scheme. As mentioned in Chapter 1, full-scale (global) blade models are not usually refined enough to predict critical detail region (local) performance. This is a problem, since damage may initiate at these sites. A combined global/local approach (Fig. 13) seems to be the evolving design methodology for skin-stiffened structures [3, 7, 10]. In this approach the loading conditions from the global model are transferred to smaller substructure models that appear to be "hotspots" for stresses. This is performed until adequate detail is incorporated into the models to predict such items as initial damage loads and location, and damage tolerance. This knowledge allows the designer to make necessary changes to the local and/or global structure, and iterate on this procedure until an acceptable design is achieved.

In the current research, testing and analysis focused on the local detail region level as part of an overall project that includes global analysis. Analytical modeling of detail regions through FEA was developed and validated with experimental results. The goals of the analytical modeling were to formulate accurate predictive capability and design methodologies for detail regions with FEA. By combining the experimental and analytical modeling, the objectives of establishing design guidelines and predictive capability for skin-stiffeners could be achieved.

Model Generation

FEA was used to model the two primary experimental specimen types used in this study, namely the double cantilever beam (DCB), and the skin-stiffener substructure (T).

The goals for the FE model of the DCB were to compare the predictions from the model, based on the VCCT techniques, with the experimentally calculated G_{Ic} values. The T specimens were modeled in order to establish predictive ability of blade substructure sections at the detail region level. It was hoped that analysis techniques could be implemented that used basic material strength and fracture data, appropriate FE models, and suitable failure criteria, to predict T specimen test results.

DCB Models

The DCB was modeled with a 2-D plane strain analysis using 8-node quadrilateral elements (plane 82) in the ANSYS 5.3 finite element code (Fig. 20). Half symmetry was used at the specimen thickness mid-plane to simplify the model. The load was applied as a nodal force at the upper left corner node which was restricted to translate in the vertical direction only. The symmetry condition was enforced by restraining all nodes along the mid-plane, up to the crack tip, with zero displacement in the y-direction. The crack length (a) was set by picking a node with appropriate coordinates in the x-direction to create a specified debond length. The mesh sizing was varied to find the mesh sensitivity of the VCCT techniques. This is discussed further in the Analytical Results section of Chapter 6. Typically, the DCB had 4 elements through the half-thickness, with the elements surrounding the crack tip highly refined to capture the stress gradients at the crack tip. Typical material properties [1] used for the D155 and DB120 fabric layers in the FE models are shown in Tables 4 and 5.

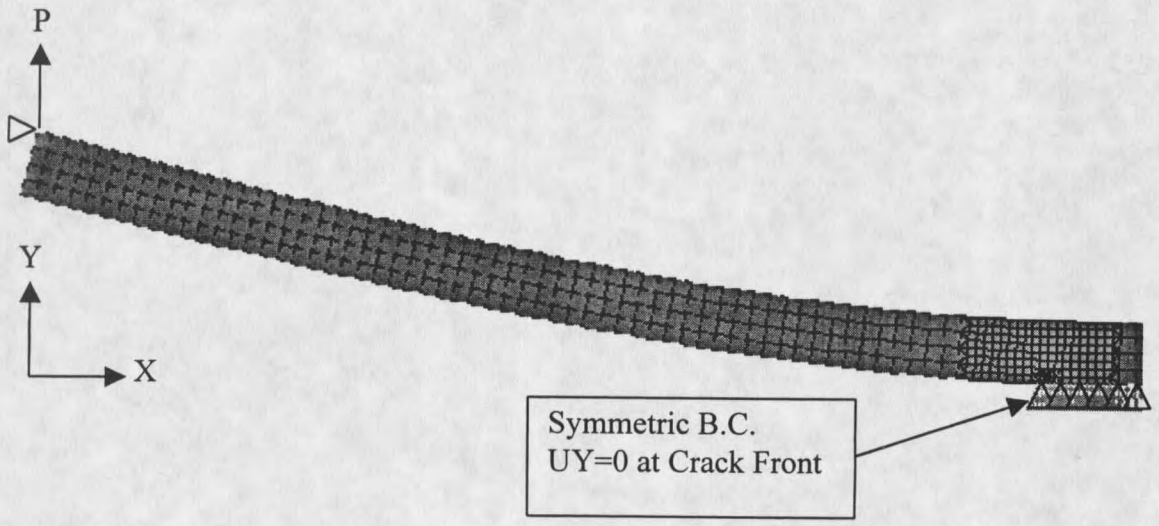

Figure 20. Deformed finite element mesh of DCB specimen with a delamination.

In order to input the properties into ANSYS correctly for the 2-D model, the relations for Poisson's major and minor ratios were implemented. This was necessary to correctly change the material properties from the axes used for material testing, to the various ply orientations in the model. This involved simply changing E_x (E_L) etc. from the material property axes, to the appropriate local direction in each layer of the FE model. When doing this, the major Poisson's ratios (ν_{12}, ν_{23}, ν_{13}) and the minor Poisson's ratios (ν_{21}, ν_{32}, ν_{31}) must be treated correctly. These values are related according to Equation 6 [37], due to compliance symmetry in the constitutive properties.

$$\nu_{ij} / E_i = \nu_{ji} / E_j \qquad (6)$$

If these ratios are not properly applied, a built-in material-checking feature in ANSYS will not allow the model to be solved, due to a lack of positive definite properties. If a

Table 4. Elastic Constants and Strengths for Unidirectional Material D155 at a $V_F = 36\%$ [1].

Physical Elastic Constants of Material D155, $V_F = 36\%$			
Property and test plane	Test Values	Average	s.d.
E_L,(LT plane),GPa	28.1, 27.0, 29.8	28.3	1.4
E_L, (LZ plane), GPa	28.0, 28.3, 27.6	28.0	0.4
E_T, (TZ plane), GPa	8.00, 7.31, 7.93	7.75	0.38
E_Z, (ZX plane), GPa	7.10, 7.65, 7.38	7.38	0.28
υ_{LT}	0.329, 0.320, 0.301	0.32	0.01
υ_{LZ}	0.305, 0.338, 0.331	0.33	0.02
υ_{TZ}	0.466, 0.395, 0.449	0.44	0.04
G_{LT}, GPa	3.31, 3.35, 3.23	3.30	0.06
G_{LZ}, GPa	3.03, 2.72, 2.70	2.82	0.19
G_{TZ}, GPa	2.78, 3.12, 1.76	2.55	0.71
Ultimate Strengths of Material D155, $V_F = 36\%$			
Property and test plane	Test Values	Average	s.d.
UTS_L, (LT plane), MPa	891, 814, 883, 838	856	37
UTS_L, (LZ plane), MPa	679, 672, 685, 646	671	17
UTS_T, (TZ plane), MPa	26.6, 36.0, 30.4, 32.9, 29.0	31.0	3.6
UTS_Z, (ZT plane), MPa	21.7, 18.7, 20.4, 18.1	19.7	1.6
UTS_Z, (ZL plane), MPa	19.4, 17.7, 22.3, 17.1, 15.2	18.4	2.7
τ_{LT}, MPa	95.1, 82.1, 78.8	85.3	8.7
τ_{LZ}, MPa	79.6, 77.3, 77.1, 63.2	74.3	7.5
τ_{TZ}, MPa	19.9, 17.6, 12.0	16.5	4.0

*Shear properties listed were determined by notched beam, ASTM D5379

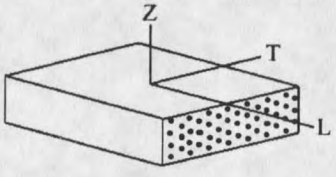

Table 5. Static longitudinal, transverse, and simulated shear properties for D155 and DB120 unidirectional materials [1].

			Longitudinal Direction									Transverse Direction			
			Elastic Constants				Tension		Compression		Shear	Tension		Compression	
Fabric	Lay-up	V_F %	E_L GPa	E_T GPa	ν_{LT}	G_{LT} GPa	UTS_L MPa	ε_U %	UCS_L MPa	ε_U %	τ_{TU} MPa	UTS_T MPa	ε_U %	UCS_T MPa	ε_U %
D155	$[0]_6$	45	37.0	8.99	0.31	4.10	986	2.83	-746	-2.02	94.2	27.2	0.30	-129	-1.67
DB120*	$[0]_{16}$	44	26.5	7.52	0.39	4.12	610	2.49	-551	-2.08	84.9	24.9	0.33	-90.8	-1.21

Notes: E_L - Longitudional modulus, ν_{LT} - Poisson's ratio, G_{LT} and τ_{TU} - Shear modulus and ultimate shear stress from a simulated shear (±45) ASTM D 3518 test. UTS_L - Ultimate longitudinal tensile strength, ε_U - Ultimate tensile strain, UCS_L - Ultimate longitudinal compressive strength, ε_U - Ultimate compressive strain.
Coupons had a 100 mm gage length with a 0.02 mm/s testing velocity. * DB120 fabric was separated into a +45 and a -45 orientation and then rotated to 0 degrees to form a unidirectional material

DCB specimen had different fabric types in the same model, a separate area represented each fabric layer. The orthotropic material properties for the fabric were then attributed to that area before mesh generation to ensure proper lay-up in the model.

Both the VCCT-1 and VCCT-2 techniques were applied to the DCB models to calculate G_{Ic} and determine mesh sensitivity for both methods as presented in Chapter 2.

Substructure Models

FEA models were created for both the thick and thin flange T specimens. They consisted of a 2-D plane strain analysis with 8-node quadrilateral (Plane 82) element types. The plane strain assumption has been used by other investigators to model skin-stringer debonding [3, 8-10, 29]. Half symmetry about the vertical mid-line of the web was used to simplify the models (Figs. 21 and 22) by restricting the nodes along the mid-line to have zero x-displacement. The support from the test fixture bar was modeled as a condition of no y-displacement at a nodal position of x = 6.35 cm on the top of the skin. The applied force observed in the experimental results was normalized per unit of specimen width and divided by two to get the load applied to the half-model. This load was applied as a nodal force in the y-direction at the top centerline of the web.

The thick flange models were analyzed to predict initial damage at the flange tip and delamination growth along the skin-flange interface. Along the delamination interface, plies were modeled individually for each of the four plies on either side of the interface. In the localized region of the delamination front, each ply layer had at least four elements through its thickness. In some cases, even more elements were used to

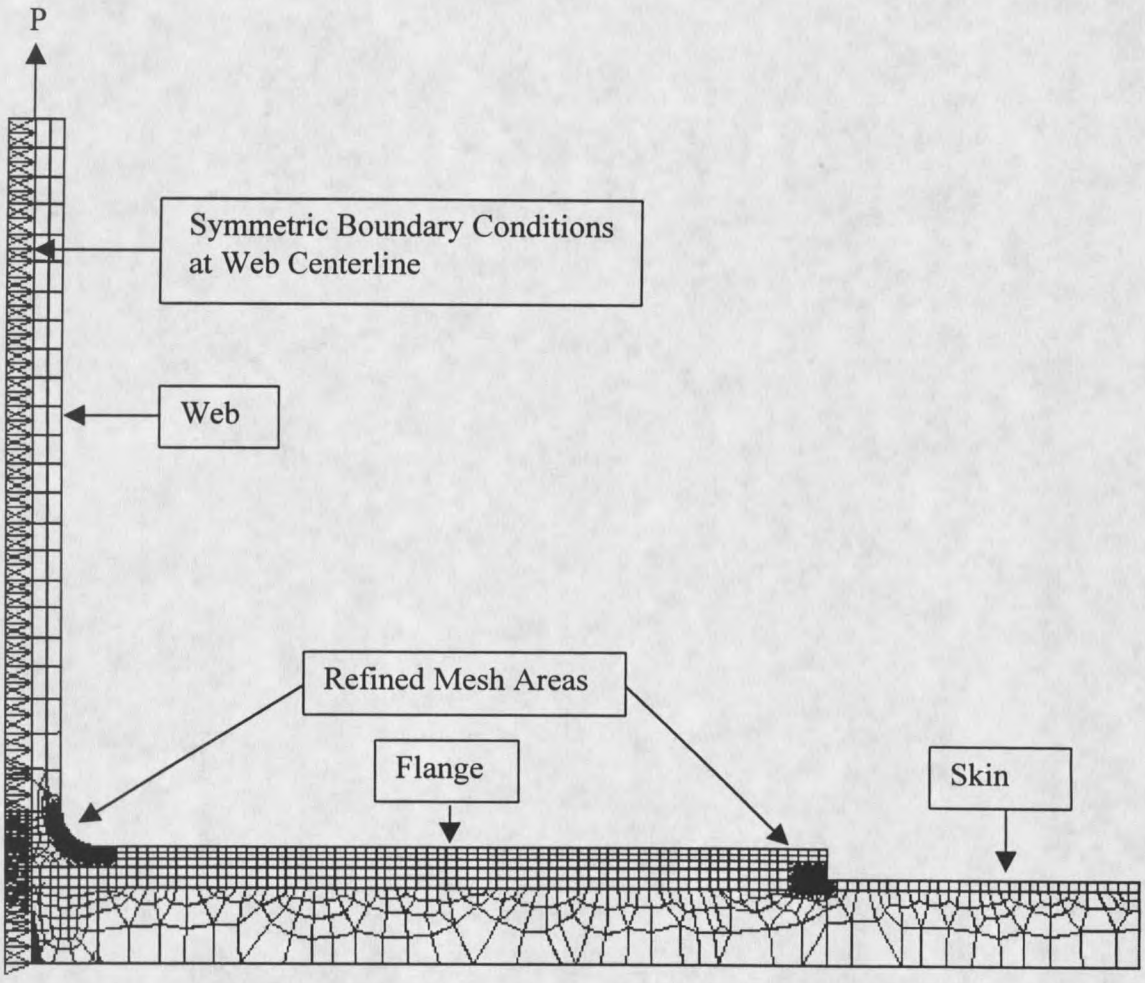

Figure 21. Finite element mesh for thin-flanged stiffener tests.

do mesh size analysis. The flange tip area was highly refined (Fig. 22) to investigate damage onset with very small initial crack lengths.

The thin flange models had the plies modeled individually in the flange section as well as in the top ply of the skin. The flange tip and bend region had highly refined meshes (Fig. 21) for analyzing strain energy release rates and strain values for use in

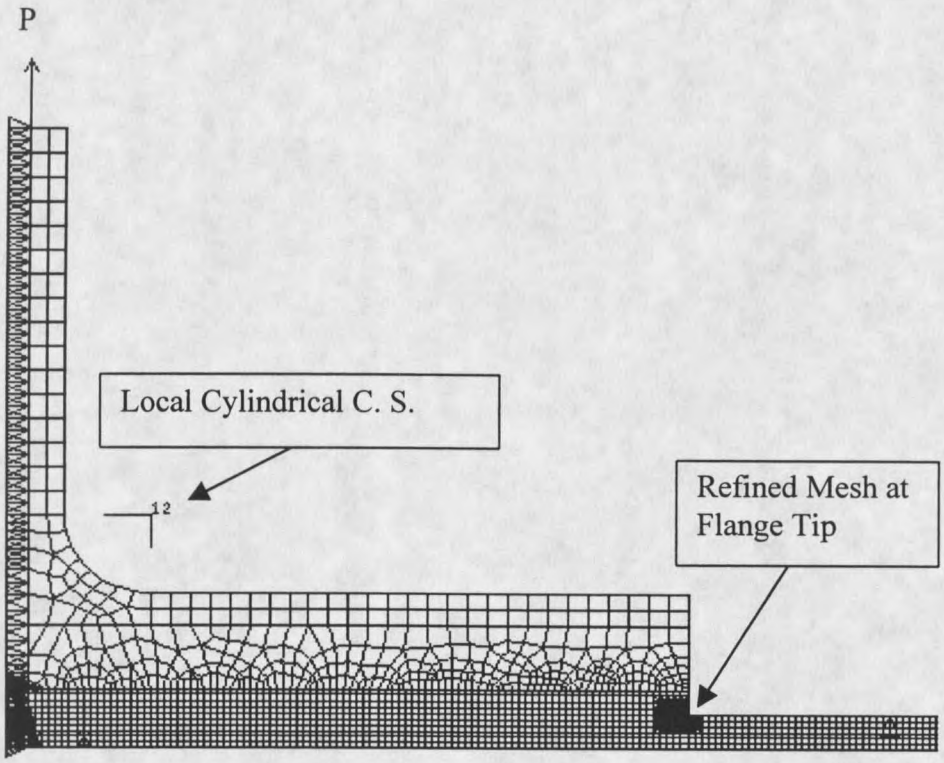

Figure 22. Finite element mesh for thick-flanged stiffener tests.

damage onset predictions.

In both model types, larger areas were created away from the crack interface that utilized smeared composite properties derived from classical laminated plate theory. This made the models more efficient while still capturing key information in the areas of interest. This was permissible since the through-thickness stresses and stress gradients were expected to decrease away from the flange tip and bend region areas as observed by Minguet et al. [8]. The delamination interface was created by modeling the stiffener and flange as separate entities, and then using multi-point constraints at the coincident nodes

to tie the skin-stiffener together. In this way, any length of delamination could be modeled by adding or deleting coupled nodal pairs.

A local cylindrical coordinate system was created at the center of the radius of curvature of the web-flange fillet area for both stiffener types. This was necessary to make the ply material properties follow the curved contour. The element coordinate systems in the bend are defined to match the local system in this area. In order to ensure that the element material properties were properly attributed, an FEA solution with this local system was benchmarked against a closed-form solution for a curved member under flexural loading.

The analysis of the specimens with FEA involved using models without a crack to simulate initial behavior in the undamaged state, and then introducing a delamination to perform fracture mechanics analysis on the debonded configuration. The intact models were checked for regions of high stress gradients or singular zones at the experimentally observed initial damage load to show which areas were prone to initial damage and delamination growth. Next, delaminations were modeled at these areas, and G values were calculated. Using the procedure outlined in Chapter 2 and Appendix A for mixed-mode growth, the load to propagate a delamination at the interface was calculated.

One problem that designers encounter with skin-stiffener intersections is trying to apply strength-based failure criteria in regions where a stress singularity exists, such as at the flange tip region. In this region, the peel stress becomes unbounded at the flange termination, as previously discussed. Moreover, as the element size is refined, the stress keeps increasing with every refinement [3], making standard stress-based analysis

useless. One approach is the "Whitney-Nuismer average stress criterion" [37], which says that fracture will occur when the average stress in a region over some characteristic distance (a_0) reaches the peel strength of the material (σ_0). The formula for the integral average stress used to calculate a_0 is presented in Equation (7).

$$\sigma_0 = \sigma_{a_0} = \frac{1}{a_0}\int_0^{a_0} \sigma_y(r,0)\,dr \qquad (7)$$

Where σ_0 = the ultimate peel strength of the material.

σ_{ao}= the average stress over distance a_0

σ_y = the peel stress distribution in the material

The material characteristic distance must be found experimentally for each material system [11, 37].

A method based on fracture mechanics was developed in this study to predict delamination onset loads. This method reduces the crack length to a very small initial value (a_i) and compares the FEA output G values to the interlaminar fracture toughness data. The load calculated to propagate this very small crack is assumed to approach the load to initiate a crack in the structure from the undamaged state. This method was applied to the singularity zone at the flange tips in the stiffener specimens to predict fracture onset.

After successfully using this technique in the present study, it was discovered that Martin [3] had previously used a similar method for predicting fracture initiation with

good results. However, as the crack length approached zero ($a < 0.25$ mm), the FEA results for G_I and G_{II} began to diverge. The results were stable and quite converged, however, at crack lengths between 0.25 mm and 0.4 mm. He concluded that as the crack became very small, the assumption that (a/da) was large was violated, and poor results were obtained.

Martin did not report any proposed range of ratios for (a/da) to use with this method of predicting fracture onset. But, based upon Martin's results and the previous recommendation [27] for (a/da) ratios with FEA of 50 to 200, it appears that this method should provide satisfactory results if the (a/da) ratio is large enough, and the modeled crack length is below 0.4 mm. The trade-off is between making the crack small enough that fracture onset is modeled properly, while maintaining a high enough (a/da) ratio that the assumptions of the crack closure integral are not violated. These parameters are investigated further in the Numerical Results section of Chapter 6.

CHAPTER 5

EXPERIMENTAL RESULTS AND DISCUSSION

This chapter summarizes the results of the experimental test methods for the DCB, ENF, and substructure test specimens. Full results are presented in Appendix B. The DCB and ENF specimens were used to examine interlaminar fracture toughness for basic material property characterization. Results are given for the delamination resistance of common interface lay-ups. The substructure test specimen results are then presented for variations in manufacturing method, matrix material, ply orientation, stiffener geometry, and applied loading.

DCB Specimens

DCB Mode I fracture toughness (G_{Ic}) tests were conducted on specimens varying in delamination interface ply orientation and delamination length. Cracks were propagated between (+45/-45) and (0/0) ply orientations to investigate toughness changes with different lay-ups. In addition, G_{Ic} values calculated with the Area and MBT methods (see Chapter 2) were compared for identical cases.

(+45/-45) Interface

The $[(+45/-45)]_{10}$ specimens showed both higher values of G_{Ic} and larger discrepancies in values calculated from the Area and MBT methods when compared with

the $[(0)]_{10}$ specimens (Figs. 23 and 24 and Table 6). The horizontal axis (crack extension (a*)) is the crack length beyond the Teflon starter film insert. The initiation value right from the starter film tip is a* = 0. The increase in G_{Ic} with increasing crack

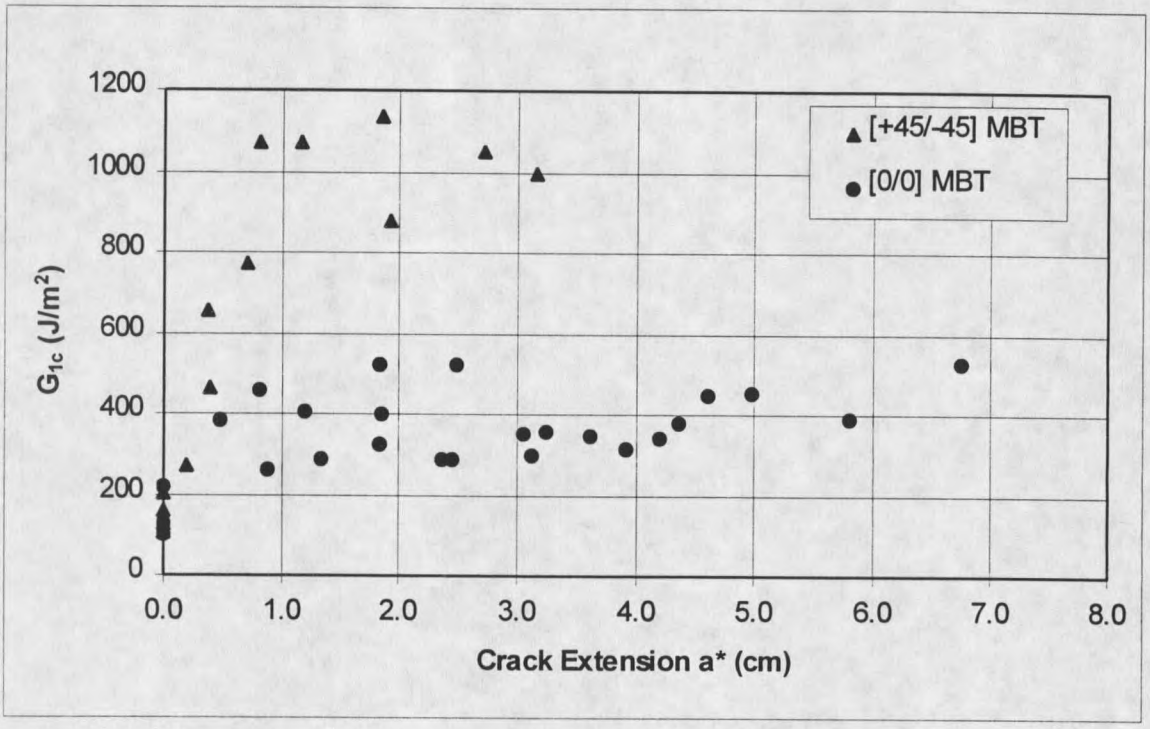

Figure 23. R-curve for (+45/-45) and (0/0) specimens calculated with the MBT method.

extension and the fact that the Area method produced consistently higher values for G_{Ic} is shown in Figure 24. G_{Ic} values for the MBT method increased from an average initiation value (at a*=0) of 140 ($\pm$ 41) J/m^2 to an average value of 1028 ($\pm$ 97) J/m^2 once the crack had grown beyond 1 cm in length. For use in FEA predictive analysis, a linear curve fit was applied to the portion of the MBT R-curve between 0 and 1 cm. For crack lengths greater than 1 cm, a horizontal line equal to the average of the data points in that range (1028 J/m^2) was used.

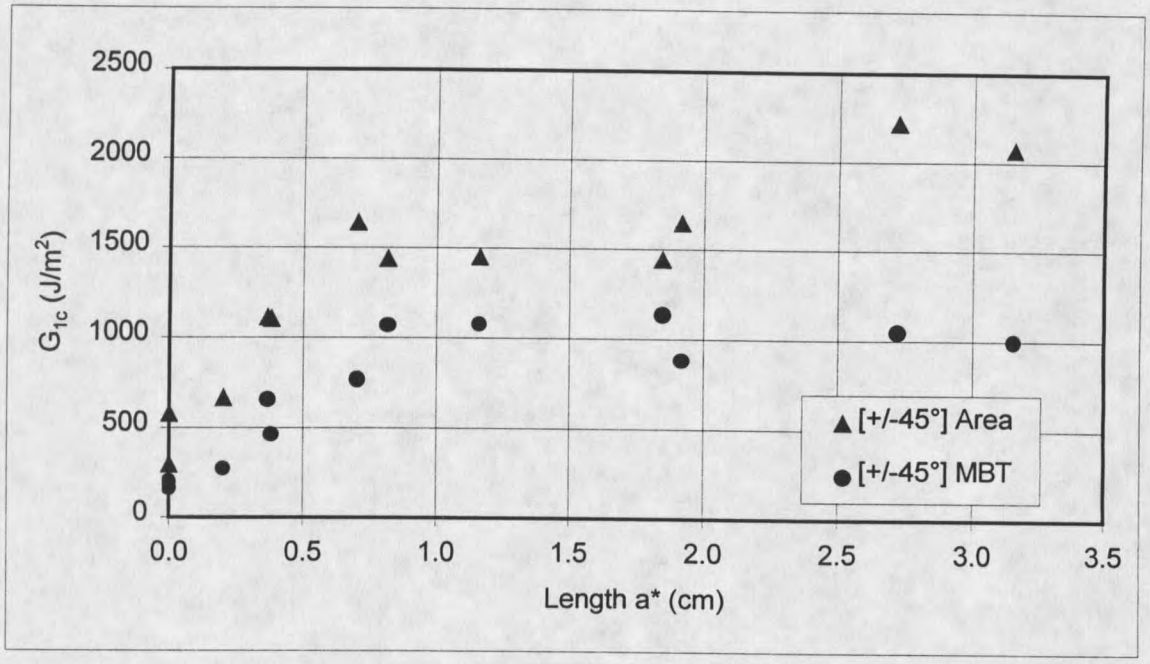

Figure 24. R-curve for (+45/-45) specimens calculated with the Area and MBT methods.

Table 6. DCB test results summary.

DCB Lay-up	# specimens	G_{Ic} (J/m^2) Initiation	Std. Dev.	# data points	G_{Ic} (J/m^2) (a*>1.0 cm)	Std. Dev.	# data points
$[(0)]_{10}$	5	138	56	4	379	81	19
$[(+45/-45)]_{10}$	2	140	41	5	1028	97	5

For the Area method, G_{Ic} values were 435 ($\pm$ 199) J/m^2 at small crack lengths, roughly 1500 J/m^2 at a crack length of 1 cm, and over 2000 J/m^2 at a length of 3 cm (Fig. 24). It should be noted that the Area method does not give a value for G_{Ic} at initiation from the starter film since the crack is extended some finite amount during the test. However, the MBT method does provide a value for G_{Ic} at initiation from the film (a*=0).

Specimens with a $[(0)_2/(+45/-45)/(+45/-45)/(0)_2]$ lay-up were also tested. These specimens provided good data points for the initiation value from the starter film tip.